Galactic angular momentum in the IllustrisTNG simulation – I. Connection to morphology, halo spin, and black hole mass

Vicente Rodriguez-Gomez [1,2]★ Shy Genel,[3,4] S. Michael Fall,[5] Annalisa Pillepich [6]
Marc Huertas-Company,[7,8] Dylan Nelson [9] Luis Enrique Pérez-Montaño,[2] Federico Marinacci [10]
Rüdiger Pakmor [11] Volker Springel,[11] Mark Vogelsberger [12] and Lars Hernquist[13]

[1]*Department of Physics & Astronomy, Johns Hopkins University, 3400 N. Charles Street, Baltimore, MD 21218, USA*
[2]*Instituto de Radioastronomía y Astrofísica, Universidad Nacional Autónoma de México, Apdo. Postal 72-3, 58089 Morelia, Mexico*
[3]*Center for Computational Astrophysics, Flatiron Institute, 162 5th Avenue, New York, NY 10010, USA*
[4]*Columbia Astrophysics Laboratory, Columbia University, 550 West 120th Street, New York, NY 10027, USA*
[5]*Space Telescope Science Institute, 3700 San Martin Drive, Baltimore, MD 21218, USA*
[6]*Max-Planck-Institut für Astronomie, Königstuhl 17, D-69117 Heidelberg, Germany*
[7]*Departamento de Astrofísica, Instituto de Astrofísica de Canarias, Universidad de La Laguna, E-38200 La Laguna, Spain*
[8]*LERMA, Observatoire de Paris, CNRS, PSL, Université Paris Diderot, F-75013 Paris, France*
[9]*Universität Heidelberg, Zentrum für Astronomie, Institut für theoretische Astrophysik, Albert-Ueberle-Straße 2, D-69120 Heidelberg, Germany*
[10]*Department of Physics & Astronomy 'Augusto Righi', University of Bologna, via Gobetti 93/2, I-40129 Bologna, Italy*
[11]*Max-Planck-Institut für Astrophysik, Karl-Schwarzschild-Straße 1, D-85741 Garching bei München, Germany*
[12]*Department of Physics, Kavli Institute for Astrophysics and Space Research, Massachusetts Institute of Technology, Cambridge, MA 02139, USA*
[13]*Harvard-Smithsonian Center for Astrophysics, 60 Garden Street, Cambridge, MA 02138, USA*

ABSTRACT

We use the TNG100 simulation of the IllustrisTNG project to investigate the stellar specific angular momenta (j_*) of ∼12 000 central galaxies at $z = 0$ in a full cosmological context, with stellar masses (M_*) ranging from 10^9 to 10^{12} M$_\odot$. We find that the j_*–M_* relations for early-type and late-type galaxies in IllustrisTNG are in good overall agreement with observations, and that these galaxy types typically 'retain' ∼10–20 and ∼50–60 per cent of their host haloes' specific angular momenta, respectively, with some dependence on the methodology used to measure galaxy morphology. We present results for *kinematic* as well as *visual-like* morphological measurements of the simulated galaxies. Next, we explore the scatter in the j_*–M_* relation with respect to the spin of the dark matter halo and the mass of the supermassive black hole (BH) at the galactic centre. We find that galaxies residing in faster spinning haloes, as well as those hosting less massive BHs, tend to have a higher specific angular momentum. We also find that, at fixed galaxy or halo mass, halo spin and BH mass are anticorrelated with each other, probably as a consequence of more efficient gas flow towards the galactic centre in slowly rotating systems. Finally, we show that halo spin plays an important role in determining galaxy sizes – larger discs form at the centres of faster rotating haloes – although the trend breaks down for massive galaxies with $M_* \gtrsim 10^{11}$ M$_\odot$, roughly the mass scale at which a galaxy's stellar mass becomes dominated by accreted stars.

Key words: methods: numerical – galaxies: formation – galaxies: haloes – galaxies: kinematics and dynamics – cosmology: theory.

1 INTRODUCTION

The angular momentum (J) of a galaxy is one of its most fundamental properties, along with its mass (M) and energy. However, while energy is largely dissipated in the form of radiation during the formation of a galaxy, its mass and momentum are approximately conserved (Fall & Efstathiou 1980). A related quantity, the *specific angular momentum* ($j = J/M$), can be used to normalize out the amount of material and thus help to understand the interplay between the various components of a galaxy, such as its gas and stars, as well

as to establish a connection to the spin of the dark matter (DM) halo, which is acquired via tidal torques from neighbouring structures in the early Universe (Peebles 1969; Doroshkevich 1970; White 1984).

In this context, Fall (1983) presented observational estimates of the stellar specific angular momenta (j_*) of a sample of nearby spiral and elliptical galaxies, and plotted them as a function of their stellar masses (M_*). He found that spiral and elliptical galaxies occupy approximately parallel tracks on the j_*–M_* diagram (on a log–log scale) with a logarithmic slope of ∼0.7 but with a large offset, such that ellipticals had lower j_* at fixed M_* than spirals by a factor of ∼6. This subject has been revisited using updated observations in a series of papers (Romanowsky & Fall 2012; Fall & Romanowsky 2013, 2018) and the original findings from Fall

★ E-mail: vrodgom.astro@gmail.com

(1983) have been approximately maintained, with the latest iteration reporting a logarithmic slope of 0.67 ± 0.07 and an offset between 'pure' discs and bulges of a factor of 8 ± 2 (Fall & Romanowsky 2018).

Other observational works have also studied the j_*–M_* diagram in the local Universe, although these are generally limited to late-type morphologies (e.g. Obreschkow & Glazebrook 2014; Lapi, Salucci & Danese 2018b; Posti et al. 2018b; Di Teodoro et al. 2021; Mancera Piña et al. 2021a, b; Hardwick et al. 2022) or consider measurements of j_* confined to relatively small apertures, of about one effective radius (Cortese et al. 2016; Tabor et al. 2019). Measuring the total j_* for elliptical galaxies remains difficult due to their more extended angular momentum profiles, and would benefit from more kinematic data out to ∼5 effective radii and beyond (Romanowsky & Fall 2012).

On the numerical side, early hydrodynamic cosmological simulations suffered from the so-called 'angular momentum catastrophe' (Navarro, Frenk & White 1995; Navarro & Steinmetz 1997), in which baryons condensed too efficiently into their nearest gravitational potential well, and most of the baryonic angular momentum was transferred to the DM halo via the strong merging activity of these baryonic clumps. It soon became clear that the key to solving this problem was to include efficient stellar feedback at early times (Sommer-Larsen, Gelato & Vedel 1999; Thacker & Couchman 2001), which reheats gas into an extended reservoir that can then cool more gradually into the central galaxy, a phenomenon sometimes referred to as a galactic fountain. The numerical treatment of hydrodynamics has also been shown to make a difference in the angular momentum content of cosmologically simulated galaxies (Torrey et al. 2012).

Using hydrodynamic cosmological simulations, only recently has it been possible to produce a statistically significant galaxy *population* with realistic amounts of angular momentum (Genel et al. 2015; Pedrosa & Tissera 2015; Teklu et al. 2015; Zavala et al. 2016; DeFelippis et al. 2017; Lagos et al. 2017, 2018), due to enormous improvements in computational capability and galaxy formation modelling (see Somerville & Davé 2015; Naab & Ostriker 2017; Vogelsberger et al. 2020, for reviews). The j_*–M_* diagram has also been addressed with zoom-in hydrodynamic simulations, which model relatively small galaxy samples at higher resolution (Obreja et al. 2016, 2019; Grand et al. 2017, 2019; Sokołowska et al. 2017; El-Badry et al. 2018), as well as with analytic, semi-analytic, and semi-empirical models (Dutton & van den Bosch 2012; Romanowsky & Fall 2012; Stevens, Croton & Mutch 2016; Shi et al. 2017; Lapi et al. 2018a; Posti et al. 2018a; Zoldan et al. 2018; Irodotou et al. 2019).

In order to understand the role of angular momentum in galaxy formation, it is often useful to define the specific angular momentum 'retention fraction,' usually denoted by f_j, which quantifies the ratio between the *specific* angular momentum of the galaxy and that of its parent halo. Traditionally, some analytic and semi-analytic models (e.g. Fall & Efstathiou 1980; Dalcanton, Spergel & Summers 1997; Avila-Reese, Firmani & Hernandez 1998; Mo, Mao & White 1998; Firmani & Avila-Reese 2000, 2009) have assumed that $f_j = 1$ for spiral galaxies, which is close to currently accepted values. Recent observational studies indicate $f_j \approx 0.7$–0.8 for spirals (Fall & Romanowsky 2013; Posti et al. 2019b; Di Teodoro et al. 2021) and $f_j \approx 0.1$ for ellipticals (Fall & Romanowsky 2013, 2018).

Some possible reasons for a 'loss' in angular momentum include gas stripping (in dense environments), gas ejection by galactic outflows (if the expelled gas comes from the outer, more angular momentum-rich regions of the galaxy), as well as so-called *biased collapse* scenarios (van den Bosch 1998; Dutton & van den Bosch

2012; Kassin et al. 2012), in which the galaxy forms preferentially from material in the inner, more angular momentum-poor regions of the halo. On the other hand, gains in angular momentum can be induced by galactic fountains, as discussed above. Other processes can result in either a loss or gain of angular momentum, such as mergers (Fall 1979; Barnes 1988; Hernquist & Mihos 1995; Springel & Hernquist 2005) and misaligned gas accretion (Sales et al. 2012).

In particular, Genel et al. (2015) investigated the stellar angular momenta of galaxies in the Illustris simulation (Genel et al. 2014; Vogelsberger et al. 2014a, b) and found that, at fixed stellar mass, late-type galaxies have higher j_* than early-type galaxies, with retention fractions of approximately 1 and 0.3, respectively. In addition, Genel et al. (2015) explored variations in galactic angular momentum with respect to modifications to the fiducial galaxy formation model, finding that stronger feedback from galactic winds results in higher galactic angular momentum, while stronger feedback from supermassive BHs acts in the opposite direction.

In this paper, we revisit the topic of galactic angular momentum from the perspective of hydrodynamic cosmological simulations, specifically using the state-of-the-art TNG100 simulation of the IllustrisTNG project (Marinacci et al. 2018; Naiman et al. 2018; Nelson et al. 2018; Pillepich et al. 2018b; Springel et al. 2018). Previous works have shown that the IllustrisTNG model returns observationally consistent correlations among galaxy stellar morphology, galaxy mass, and star formation rate at low redshift (Huertas-Company et al. 2019; Rodriguez-Gomez et al. 2019; Tacchella et al. 2019; Donnari et al. 2021a, b), as well as the redshift evolution of the morphological fractions and of the degree of rotational versus dispersion-supported motions (Pillepich et al. 2019; Varma et al. 2022). Here, we focus on how j_* relates to galaxy stellar morphology, to the spin of the DM halo, and to the mass of the central black hole (BH) over a wide range of stellar masses ($M_* = 10^9$–10^{12} M$_\odot$) at $z = 0$. We also discuss the retention fraction f_j in the context of galaxy morphology, and determine whether the relation between halo spin and galaxy size predicted by some theoretical models arises naturally in IllustrisTNG.

This paper is structured as follows. In Section 2, we describe the simulation used for this work, provide details about the main calculations, and define the galaxy sample. Section 3 contains our main results, which comprise a study of the interplay between j_*, f_j, and galaxy morphology (Section 3.1), an analysis of the role of halo spin and BH mass in establishing galactic angular momentum (Section 3.2), and an exploration of the link between halo spin and galaxy size (Section 3.3). Finally, in Section 4 we discuss these results and present our conclusions.

2 METHODOLOGY

2.1 The IllustrisTNG simulation suite

The IllustrisTNG project (Marinacci et al. 2018; Naiman et al. 2018; Nelson et al. 2018, 2019b; Pillepich et al. 2018b, 2019; Springel et al. 2018) is a suite of magnetohydrodynamic cosmological simulations carried out with the moving-mesh code AREPO (Springel 2010; Pakmor & Springel 2013; Pakmor et al. 2016), featuring a galaxy formation model that includes prescriptions for radiative cooling, star formation and evolution, metal enrichment, supernova feedback, and supermassive BH growth and feedback (Weinberger et al. 2017; Pillepich et al. 2018a). We provide more details about the numerical implementation of these physical processes in Section 2.2.

In this work, we use the highest resolution version of the TNG100 simulation (TNG100-1), which covers a periodic volume

of $(75h^{-1}\,\text{Mpc})^3 \approx (110.7\,\text{Mpc})^3$ and follows the evolution of 1820^3 DM particles and approximately 1820^3 baryonic resolution elements (gas cells and stellar particles), which have masses of 7.47×10^6 and $1.39 \times 10^6\,\text{M}_\odot$ (on average), respectively. The gravitational softening length for both DM and stellar particles is $0.5h^{-1} \approx 0.74\,\text{kpc}$ at $z = 0$, while for gas cells it is tied to their radius and in principle can be as low as 0.19 kpc.

Haloes and subhaloes are identified with the friends-of-friends (FoF, Davis et al. 1985) and SUBFIND (Springel et al. 2001; Dolag et al. 2009) algorithms, respectively. We define galaxies as being composed of the stellar and star-forming gas components of subhaloes. Unless otherwise noted, we measure all properties of a galaxy (e.g. stellar mass or angular momentum) for the entire SUBFIND object, i.e. without removing the particles found beyond some fiducial aperture (e.g. twice the stellar half-mass radius).

The initial conditions of the simulation have been set at $z = 127$ using the N-GENIC code (Springel 2005), based on a power spectrum generated by CAMB (Lewis, Challinor & Lasenby 2000). The cosmological parameters adopted in IllustrisTNG are $\Omega_m = 0.3089$, $\Omega_b = 0.0486$, $\Omega_\Lambda = 0.6911$, $\sigma_8 = 0.8159$, $n_s = 0.9667$, and $h = 0.6774$, in accordance with Planck measurements (Planck Collaboration XIII 2016).

2.2 The galaxy formation model

Here, we summarize some of the most salient features of the IllustrisTNG galaxy formation model, which is based on the original Illustris model (Vogelsberger et al. 2013; Torrey et al. 2014). For brevity, we omit details about the gravitational and magnetohydro-dynamic calculations, and instead give an overview of the physical prescriptions for radiative cooling, star formation and evolution, metal enrichment, galactic wind feedback, supermassive BH growth, and feedback from active galactic nuclei (AGNs). For a complete description of the IllustrisTNG model, we refer the reader to Weinberger et al. (2017) and Pillepich et al. (2018a).

Gas in the simulation is allowed to cool through primordial and metal-line cooling in the presence of a redshift-dependent, spatially uniform, ionizing UV background (Faucher-Giguère et al. 2009) that is switched on at $z = 6$, taking self-shielding corrections into account (Vogelsberger et al. 2013). Gas cells with densities above $\rho_{\text{thres}} = 0.13\,\text{cm}^{-3}$ (in units of hydrogen number density) are considered to be star-forming, and become candidates to be stochastically converted into stellar particles according to the subresolution model of Springel & Hernquist (2003), with some modifications such as using a Chabrier (2003) initial mass function (IMF) instead of a Salpeter (1955) IMF, as detailed in Vogelsberger et al. (2013). This star-forming gas is modelled with a two-phase, *effective* equation of state that describes the formation and evaporation of unresolved cold clouds embedded in a hot ambient medium, including the effects of supernovae that inject metal-enriched gas and thermal energy to the ambient phase. As shown in Springel & Hernquist (2003), this model quickly leads to a self-regulated, 'quiescent' mode of star formation.

Stellar particles in the simulation represent coeval stellar populations with a Chabrier (2003) IMF. These are allowed to evolve in time while depositing mass and metals – originating from asymptotic giant branch (AGB) stars and supernovae of Types Ia (SNIa) and II (SNII) – into the surrounding gas, keeping track of the production and evolution of nine elements (H, He, C, N, O, Ne, Mg, Si, Fe). The minimum mass for a star to end its life as a core-collapse supernova (SNII) was increased from $6\,\text{M}_\odot$ in Illustris to $8\,\text{M}_\odot$ in IllustrisTNG (Pillepich et al. 2018a). Accordingly, stars less massive than $8\,\text{M}_\odot$

are assumed to enter an AGB phase. Finally, given the uncertainty about the progenitors of SNIa events, the SNIa rate is obtained from a simple delay-time distribution, regardless of the metallicity and IMF of the parent stellar population.

Galactic winds are launched (in the form of wind particles) from star-forming gas cells in a random direction with a speed that is proportional to $\sigma_{\text{DM}} H(z)^{-1/3}$, where σ_{DM} is the local, one-dimensional DM velocity dispersion and $H(z)$ is the Hubble parameter at redshift z. A velocity floor of $350\,\text{km s}^{-1}$ is also imposed, as described in Pillepich et al. (2018a). When launched, the wind particles are hydrodynamically decoupled until they leave their local interstellar medium, which typically happens when the density of the gas cell where they are currently located falls below $0.05\rho_{\text{thres}}$ (5 per cent of the density threshold for star formation), transferring their mass, momentum, metals, and energy to that gas cell. The wind mass loading factor, η_w,[1] depends on the available energy for wind generation from core-collapse supernovae (SNII), as in the original Illustris implementation (Vogelsberger et al. 2013), but now also depends on gas metallicity, such that η_w becomes smaller in higher metallicity environments. In addition, the winds are now allowed to carry a small fraction of thermal energy.

Supermassive BHs are 'seeded' at the centres of haloes that reach a FoF group mass of $5 \times 10^{10} h^{-1}\,\text{M}_\odot$. The BH seed mass is $8 \times 10^5 h^{-1}\,\text{M}_\odot$, a value that is approximately eight times larger than the seed mass in the original Illustris model. The supermassive BHs can then grow by accreting material from their surroundings, as well as by merging with other BHs. The accretion rate on to supermassive BHs is assumed to be given by the Bondi accretion rate (Bondi 1952), $\dot{M}_{\text{Bondi}}$, limited by the Eddington accretion rate, $\dot{M}_{\text{Edd}}$:

$$\dot{M}_{\text{BH}} = \min(\dot{M}_{\text{Bondi}}, \dot{M}_{\text{Edd}}), \tag{1}$$

where

$$\dot{M}_{\text{Bondi}} = \frac{4\pi G^2 M_{\text{BH}}^2 \rho}{c_s^3}, \tag{2}$$

$$\dot{M}_{\text{Edd}} = \frac{4\pi G M_{\text{BH}} m_p}{\epsilon_r \sigma_T c}. \tag{3}$$

Here, M_{BH} denotes the BH mass, G the gravitational constant, c the speed of light in vacuum, m_p the proton mass, and σ_T the Thomson cross-section. The factor ϵ_r is the radiative efficiency, which quantifies the radiated luminosity in terms of the accreted rest-mass energy ($L_r = \epsilon_r \dot{M}_{\text{BH}} c^2$), and in this model is assumed to have a fixed value of 0.2. Finally, ρ and c_s are the density and sound speed of the gas around the supermassive BH, which are calculated in a kernel-weighted fashion over a spherical region containing approximately 256 gas cells (at TNG100 resolution).

It is worth noting that current cosmological and galaxy-scale hydrodynamic simulations cannot resolve the region actually associated with the accretion disc around the supermassive BH, by several orders of magnitude. This led some early models of AGN feedback in hydrodynamic simulations (Springel, Di Matteo & Hernquist 2005; Sijacki et al. 2007) to introduce a dimensionless 'boost factor' α when calculating $\dot{M}_{\text{Bondi}}$, which was also included in the original Illustris model (Vogelsberger et al. 2013) with a value of $\alpha = 100$. This factor has been eliminated in IllustrisTNG, being effectively replaced by the larger BH seed mass mentioned above, which achieves a similar effect by promoting early BH growth (Weinberger et al. 2017).

---

[1]The wind mass loading factor is defined as $\eta_w \equiv \dot{M}_w / \dot{M}_{\text{SFR}}$, where $\dot{M}_w$ is the rate of gas mass ejected in the form of wind particles and $\dot{M}_{\text{SFR}}$ is the local star formation rate.

Once the BH accretion rate has been determined, AGN feedback can operate in two different modes depending on the accretion state: (i) a high-accretion mode, sometimes referred to as the 'quasar' mode, which corresponds to a classic accretion disc (Shakura & Sunyaev 1973), and (ii) a low-accretion mode, which operates for BHs accreting below some threshold value of the Eddington ratio, $\dot{M}_{\rm Bondi}/\dot{M}_{\rm Edd}$. In IllustrisTNG, the feedback associated with the latter mode is described with the 'kinetic wind' model of Weinberger et al. (2017), which was inspired by observational findings (e.g. the prevalence of 'red geyser' galaxies, Cheung et al. 2016) as well as theoretical considerations (e.g. Yuan & Narayan 2014), and replaces the 'radio bubble' model of Sijacki et al. (2007) that was used in Illustris.

The transition between the two AGN feedback modes takes place when the Eddington ratio ($\dot{M}_{\rm Bondi}/\dot{M}_{\rm Edd}$) reaches a threshold χ given by

$$\chi = \min\left[\chi_0\left(\frac{M_{\rm BH}}{10^8\,{\rm M}_\odot}\right)^\beta, 0.1\right], \tag{4}$$

where $\chi_0 = 0.002$ and $\beta = 2$. For BHs with $\dot{M}_{\rm Bondi}/\dot{M}_{\rm Edd} \geq \chi$, *thermal* energy is injected in a kernel-weighted fashion over the same region used to calculate the accretion rate (i.e. a sphere enclosing approximately 256 gas cells) at a rate $\dot{E}_{\rm high} = 0.02\dot{M}_{\rm BH}c^2$. Conversely, BHs with $\dot{M}_{\rm Bondi}/\dot{M}_{\rm Edd} < \chi$ impart *kinetic* energy to neighbouring gas cells (also in a kernel-weighted manner over the same spherical region) at a rate $\dot{E}_{\rm low} = \epsilon_{\rm f,kin}\dot{M}_{\rm BH}c^2$, where the efficiency $\epsilon_{\rm f,kin}$ is typically equal to its maximum value of 0.2, but decreases proportionally to ρ at sufficiently low densities ($\rho < 0.01\rho_{\rm thres}$) in order to prevent the kinetic feedback mode from pushing the densities to ever lower values. The kinetic energy is injected in the form of a momentum kick in a random direction for each injection event (Weinberger et al. 2017). This approach violates strict momentum conservation for a single injection event, but ultimately conserves momentum by averaging over many injection events. As with galactic winds, this represents an inherently isotropic feedback model.

Overall, the IllustrisTNG galaxy formation model has numerous free parameters (some of them better constrained than others) that have been calibrated to match several observables at $z = 0$ – namely, the galaxy stellar mass function, the stellar-to-halo and BH-to-halo mass relations, the halo gas fraction as a function of halo mass, and the galaxy size versus stellar mass relation – as well as the global star formation rate density at $z = 0$–8 (Pillepich et al. 2018a). We note, however, that the model was not tuned to match the angular momentum content of galaxies, nor to enforce any correlation between galactic angular momentum and other galaxy or halo properties.

2.3 Measuring angular momentum

The galaxies' stellar angular momenta are measured following Genel et al. (2015). For each subhalo, the calculation frame is centred on the particle (of any type) with the lowest gravitational potential. It is important not to set the origin at the centre of mass, which can be sensitive to structure at large radii. However, the velocity of the calculation frame coincides with that of the stellar centre of mass, which is not sensitive to the velocity of any individual particle. As mentioned in Section 2.1, these measurements are not restricted to any fiducial radius, so they are carried out for the entire SUBFIND object (accounting only for the stellar particles).

The angular momenta of the parent haloes are obtained by means of a spherical overdensity calculation equivalent to that of Zjupa & Springel (2017). For each FoF group, the calculation frame is centred on the particle with the lowest gravitational potential, while velocities are measured with respect to the centre-of-mass velocity, which is calculated by including all resolution elements (i.e. DM, gas, stars, supermassive BHs) within $R_{200} \equiv R_{200,{\rm crit}}$, i.e. the radius enclosing an average density equal to 200 times the critical density of the Universe. The magnitude of the angular momentum, $J_{200} \equiv J_{200,{\rm crit}}$, and the mass of the halo, $M_{200} \equiv M_{200,{\rm crit}}$, are also measured within R_{200}. The *specific* angular momentum of the halo is defined as $j_{200} \equiv J_{200}/M_{200}$.

Once these halo properties are known, the halo spin parameter λ (Peebles 1969) can be quantified using the closely related definition by Bullock et al. (2001),

$$\lambda' \equiv \frac{J_{200}}{\sqrt{2}M_{200}V_{200}R_{200}} = \frac{j_{200}}{\sqrt{2}V_{200}R_{200}}, \tag{5}$$

where $V_{200} = \sqrt{GM_{200}/R_{200}}$ is the circular velocity at R_{200}. The halo spin parameter is predicted to follow a lognormal distribution that is relatively insensitive to halo mass, environment, or redshift. We note that these calculations include all particles contained within R_{200}, regardless of whether they belong to the FoF group or not (see Zjupa & Springel 2017, for more details).

In previous work (Rodriguez-Gomez et al. 2017), we additionally matched each halo from the hydrodynamic simulation to its counterpart from a corresponding DM-only (DMO) run and used the spin measurement from the latter, $\lambda'_{\rm DMO}$, in order to remove any possible influence of the galaxy itself on the halo spin. Here, we do not take this extra step, having verified that none of our results changes appreciably if we replace λ' with $\lambda'_{\rm DMO}$, and instead follow the simpler approach of taking both the galaxy and halo measurements from the hydrodynamic run. This choice is also supported by Zjupa & Springel (2017), who found that the spin parameter of DM haloes is affected in a minimal way by the dissipative collapse of baryons within them.

2.4 Quantifying galaxy morphology

We employ two different measures of galaxy morphology throughout this paper. The first one is the so-called kappa parameter, $\kappa_{\rm rot}$, which quantifies the fraction of the stellar kinetic energy that is invested into ordered circular motion (Sales et al. 2010; Rodriguez-Gomez et al. 2017). More precisely, it is defined as

$$\kappa_{\rm rot} = \frac{K_{\rm rot}}{K} = \frac{1}{K}\sum_i \frac{1}{2}m_i\left(\frac{j_{z,i}}{R_i}\right)^2, \tag{6}$$

where K is the total kinetic energy of the stellar component, m_i is the mass of the i-th particle, $j_{z,i}$ is the z-component of the particle's specific angular momentum, R_i is the projected radius, and the sum is carried out over all the stellar particles in the galaxy. The z-axis is set to coincide with the stellar angular momentum of the galaxy, as defined in Section 2.3.

Like other *kinematic* measures of galaxy morphology (e.g. Abadi et al. 2003; Scannapieco et al. 2009, 2012; Aumer et al. 2013; Dubois et al. 2016), $\kappa_{\rm rot}$ is a good proxy for the amount of rotational support in a galaxy (see Rodriguez-Gomez et al. 2017, for a discussion). For example, Tacchella et al. (2019) quantified the spheroid-to-total ratio (S/T) and the concentration of the stellar mass density profile (C_{82}) of TNG100 galaxies, while Pillepich et al. (2019) quantified both structural morphologies via 3D stellar shapes as well as v/σ. Some recent works (e.g. Correa et al. 2017) use an alternative definition of

$\kappa_{\rm rot}$ where the sum in equation (6) is only carried out for corotating particles, thus excluding counterrotating stars that are probably part of the bulge (or a counterrotating disc, e.g. Starkenburg et al. 2019). For simplicity, here we maintain the original definition and do not distinguish between corotating and counterrotating particles in equation (6). A comparison between both definitions can be found in appendix A from Rodriguez-Gomez et al. (2017).

While such measures of kinematic morphology are very useful in hydrodynamic simulations, they generally cannot be directly compared to observations. Therefore, we also employ the *visual-like* morphologies presented in Huertas-Company et al. (2019), which were obtained by applying a neural network trained on visual morphologies from the Sloan Digital Sky Survey (SDSS) to synthetic images from the TNG100 simulation (Rodriguez-Gomez et al. 2019) designed to match such SDSS observations. Here, we use the first level of the binary classification hierarchy described in Huertas-Company et al. (2019), which returns the probability for a galaxy to be late-type, $P(\text{Late}) = 1 - P(\text{Early})$.

As discussed in Huertas-Company et al. (2019), galaxies with $P(\text{Late}) < 0.5$ mostly consist of elliptical and lenticular galaxies, while those with $P(\text{Late}) \geq 0.5$ include all types of spirals. Although we will later explore the variation in some quantities for galaxies with $P(\text{Late})$ values ranging continuously from 0 to 1, we note that this quantity was not designed to be used as a precise mapping for the Hubble sequence. Instead, our purpose is simply to complement our results with an alternative morphological measurement that is more observationally meaningful than $\kappa_{\rm rot}$.

Finally, we note that the DM particle mass in the TNG100 simulation, $m_{\rm DM} \approx 7.5 \times 10^6 \, {\rm M}_\odot$, exceeds the critical value of $\sim 10^6 \, {\rm M}_\odot$ for significant heating of stellar motions in galactic discs over a Hubble time (Lacey & Ostriker 1985; Ludlow et al. 2021). This spurious heating causes simulated discs to become more spheroidal (earlier morphology) and to rotate less rapidly (lower j_*). According to idealized simulations of isolated stellar discs embedded in DM haloes with particle masses similar to that of TNG100, the loss of j_* over 10^{10} yr increases from ~ 1 per cent for $M_* \sim 10^{11} \, {\rm M}_\odot$ to ~ 30 per cent for $M_* \sim 10^9 \, {\rm M}_\odot$ (Wilkinson et al., in preparation). The importance of this heating effect for the evolution of galactic discs in hydrodynamic cosmological simulations such as IllustrisTNG is now under active investigation (Ludlow et al., in preparation).

2.5 The galaxy sample

We consider all central galaxies at $z = 0$ with stellar masses M_* above $10^9 \, {\rm M}_\odot$, which represents a total of 12 235 objects. We limit this work to central galaxies because we are interested in the connection to properties of their host haloes, which would be difficult to interpret in the case of satellites. However, we note that none of our other results (i.e. the ones not involving halo quantities) would change significantly if we had included satellite galaxies as well.

When considering the visual-like morphologies from Huertas-Company et al. (2019), only galaxies with $M_* \geq 10^{9.5} \, {\rm M}_\odot$ are shown, which corresponds to the stellar mass range of the galaxies with synthetic images in Rodriguez-Gomez et al. (2019). Smaller galaxies were excluded due to the computational cost of running the SKIRT radiative transfer code (Baes et al. 2011; Camps & Baes 2015) on a larger galaxy sample. We also note that the analyses in Rodriguez-Gomez et al. (2019) and Huertas-Company et al. (2019), originally carried out for galaxies at $z \approx 0.05$ (snapshot 95 in IllustrisTNG), were afterwards repeated for galaxies at $z = 0$ (snapshot 99), but

'mock-observing' them at $z \approx 0.05$ for the sake of consistency. This extension of previous work resulted in the visual-like morphologies used for this paper.

3 RESULTS: GALACTIC ANGULAR MOMENTUM

This section contains our main results, which comprise an exploration of galactic angular momentum at $z = 0$ and its relation to morphology (Section 3.1), as well as to halo spin and BH mass (Section 3.2). We also test whether there is a correlation between halo spin and galaxy size in IllustrisTNG (Section 3.3).

### 3.1 Connection to morphology

Observations reveal that galaxies of different morphologies (or bulge fractions, B/T) follow roughly parallel scaling relations (in log–log space) between stellar specific angular momentum and stellar mass of the form $j_* \propto M_*^\alpha$, with similar indices $\alpha \approx 2/3$ but different normalizations, by a factor of ~ 8 between late-type spirals and ellipticals (Fall 1983; Romanowsky & Fall 2012; Fall & Romanowsky 2013, 2018). These scaling relations for the stellar components of galaxies are reminiscent of the one for DM haloes, $j_{200} \propto M_{200}^{2/3}\lambda$ (since the halo spin λ is essentially independent of M_{200}). Connecting the j_*–M_* and j_{200}–M_{200} relations by means of the intervening j_*–j_{200} and M_*–M_{200} relations provides some important clues about galaxy formation, as we explore in detail later in this section.

Fig. 1 shows how early-type and late-type galaxies distribute on the j_*–M_* plane, often referred to as the *Fall diagram*, comparing simulated galaxies from IllustrisTNG at $z = 0$ to observational measurements from Fall & Romanowsky (2013) in the upper panels,[2] and from Posti et al. (2018b) and Di Teodoro et al. (2021) in the lower panels.[3] We quantify the morphologies of the simulated galaxies according to the two different methods described in Section 2.4. On the left-hand panels, IllustrisTNG galaxies are separated according to the $\kappa_{\rm rot}$ parameter (Sales et al. 2010; Rodriguez-Gomez et al. 2017), i.e. the fraction of kinetic energy contributed by the azimuthal component of the stellar velocities, while galaxies on the right-hand panels are separated by $P(\text{Late})$, the probability of having a late-type morphology according to the deep learning classifier from Huertas-Company et al. (2019). For both $\kappa_{\rm rot}$ and $P(\text{Late})$, early types are distinguished from late types by imposing a cut at a value of 0.5 (Rodriguez-Gomez et al. 2017; Huertas-Company et al. 2019), as indicated by the figure labels.

The quantities $\kappa_{\rm rot}$ and $P(\text{Late})$ are examples of *kinematic* and *visual-like* morphologies, respectively, and we will consider both types of measurement throughout the rest of this paper in order to reduce the dependence of our results on any particular type of morphological measurement, as well as to reflect the fact that galaxy morphologies in hydrodynamic cosmological simulations are not yet in perfect agreement with observations (e.g. Snyder et al. 2015; Bottrell et al. 2017; Rodriguez-Gomez et al. 2019).

---

[2]Fall & Romanowsky (2013) revised the original j_*–M_* data of Romanowsky & Fall (2012) using more accurate mass-to-light ratios and listed these revisions in table 1 of Fall & Romanowsky (2018). The last of these papers also presents the power-law fits to the revised j_*–M_* data that we use here.
[3]Three lenticular (S0) galaxies were removed from the sample by Posti et al. (2018b), so that it consists only of late-type galaxies.
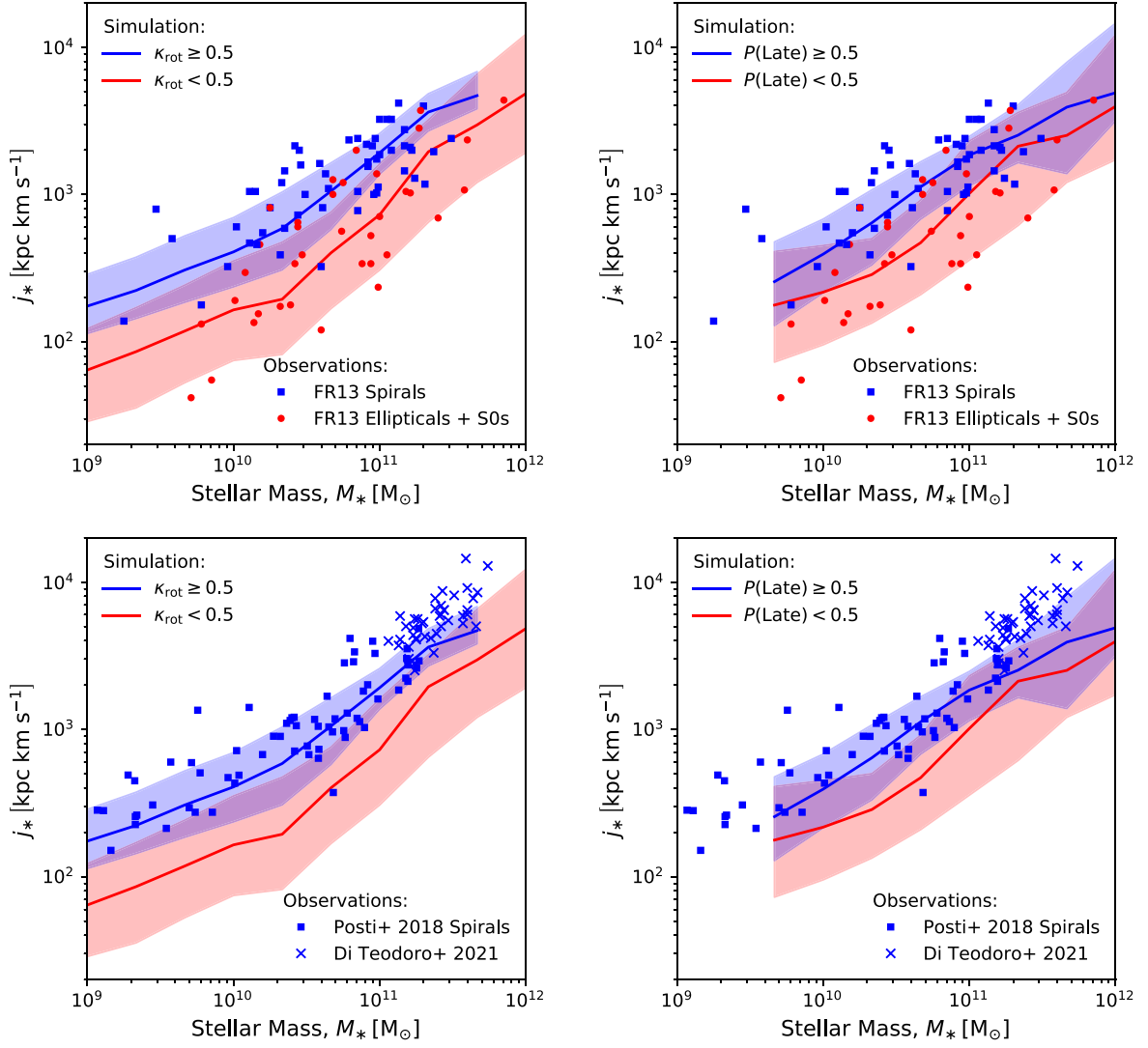
Figure 1. Stellar specific angular momentum (j_*) as a function of stellar mass (M_*) for central galaxies from the IllustrisTNG simulation at $z = 0$. The red and blue lines show median trends for early-type and late-type galaxies, respectively, while the shaded regions represent the corresponding 16th to 84th percentile ranges at fixed stellar mass. On the left-hand panels, galaxies are classified according to *kinematic* morphology, using the κ_{rot} parameter (Sales et al. 2010), while on the right-hand panels they are separated according to *visual-like* morphology, using a deep-learning algorithm (Huertas-Company et al. 2019). On the top panels, the blue squares show observational j_* estimates for spiral galaxies by Fall & Romanowsky (2013), while the red circles show the corresponding measurements for elliptical and lenticular (S0) galaxies. On the bottom panels, the blue symbols represent observational estimates by Posti et al. (2018b) and Di Teodoro et al. (2021) for spiral galaxies.

Overall, Fig. 1 shows good agreement between simulations and observations, except perhaps for the sample of extremely massive spirals from Di Teodoro et al. (2021), which have somewhat higher j_* values than our simulated galaxies. Other hydrodynamic cosmological simulations have also been able to reproduce the observed j_*–M_* relation to a reasonable degree (within a factor of ~2). For example, Teklu et al. (2015) and Zavala et al. (2016) report broad agreement with observational trends in the j_*–M_* diagram for simulated galaxies from the Magneticum Pathfinder (Hirschmann et al. 2014) and EAGLE (Crain et al. 2015; Schaye et al. 2015) simulations, respectively, although in both cases they find that their simulated galaxies have slightly lower j_* values than observed galaxies. Similarly, using the original Illustris simulation (Genel et al. 2014; Vogelsberger et al. 2014a, b), Genel et al. (2015) find j_*–M_* trends in reasonable agreement with observations, although

with a somewhat shallower logarithmic slope for the late types. By comparison, the j_*–M_* trends in IllustrisTNG display even better agreement with observations in both normalization and slope.

Fig. 2 also shows the j_*–M_* plane in IllustrisTNG at $z = 0$, but in this case the simulated galaxies are separated according to their *percentile at a fixed stellar mass* in κ_{rot} (left) or P(Late) (right), where the different coloured lines correspond to 10 equally spaced percentile ranges between 0 and 100. The motivation for doing this is to remove the dependence on the actual value of each morphological classification, and instead show the variation in j_* due to the 'ranking' of galaxy morphologies in each stellar mass bin. In principle, this procedure could be mimicked in observations, effectively constituting a 'morphological matching' at fixed stellar mass. However, this approach would require j_* measurements for complete, volume-limited galaxy samples.
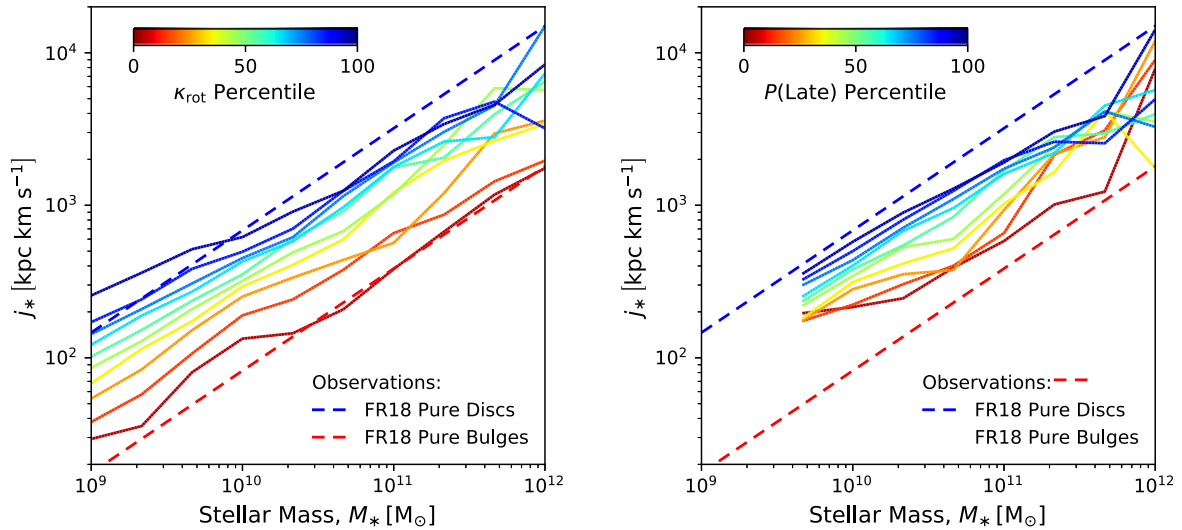
Figure 2. The j_*–M_* relation for central galaxies at $z = 0$, separating them according to the *percentile at a fixed stellar mass* of $\kappa_{\rm rot}$ (left) and $P(\rm Late)$ (right), as indicated by the colour scale. Galaxies are thus classified in a way that is less sensitive to the details of the morphological measurement, instead depending only on the relative ordering of their morphologies at a fixed stellar mass. This approach results in approximately parallel tracks on the j_*–M_* diagram for the different morphological 'types'. The blue and red dashed lines show the trends inferred from the 3D fits from Fall & Romanowsky (2018) for 'pure' discs and bulges, respectively, which have a logarithmic slope $\alpha = 0.67 \pm 0.07 \approx 2/3$.

The blue and red dashed lines in Fig. 2 represent the 3D fits from Fall & Romanowsky (2018) for 'pure' discs and bulges, respectively, which have a logarithmic slope $\alpha = 0.67 \pm 0.07 \approx 2/3$. These lines are remarkably close to the trends for IllustrisTNG galaxies in the highest (90–100) and lowest (0–10) percentile ranges, indicating that the most extreme morphological types in the simulation have similar j_* values to those of pure discs and spheroids in the observations. Close inspection of Fig. 2 also shows that the j_* trends are slightly shallower than $M_*^{2/3}$, with logarithmic slopes of ~0.5–0.6 for the various percentile intervals.

Fig. 3 is analogous to Fig. 2 except that galaxies are now split according to the actual values of $\kappa_{\rm rot}$ and $P(\rm Late)$ instead of their percentiles at a fixed stellar mass. While the trends for different $P(\rm Late)$ values (right-hand panel) are relatively unchanged, the trends for different $\kappa_{\rm rot}$ values (left-hand panel) now exhibit a bend near $M_* \sim 2$–3×10^{10} M$_\odot$, with logarithmic slopes steeper (shallower) than 2/3 for galaxies with stellar masses above (below) this transition.

The main reason for the qualitative differences between Figs 2 and 3, which are more noticeable in the case of the $\kappa_{\rm rot}$ parameter (left-hand panels), is that galaxy morphology is mass-dependent: there are more disc-dominated galaxies at $\log_{10}(M_*/{\rm M}_\odot) \sim 10.5$ and more spheroid-dominated galaxies at lower and higher masses (this trend is reproduced in IllustrisTNG, e.g. Tacchella et al. 2019). However, the fact that IllustrisTNG predicts bends for the individual galaxy types (Fig. 3) is in tension with the observations by Fall & Romanowsky (2013), which show unbent power laws. We note that Di Teodoro et al. (2021) found a slightly steeper logarithmic slope for their observational sample of 'super spirals,' such that a very gradual bend appears when combining their measurements with those of Posti et al. (2018b) (see Fig. 1), but this variation in slope is much weaker than in IllustrisTNG.

In Fig. 4, we plot the specific angular momentum 'retention fraction', defined as the ratio between the specific angular momentum of the galaxy and that of its host halo ($f_j \equiv j_*/j_{200}$), as a function of stellar mass for central galaxies at $z = 0$. As in Fig. 3, the various lines correspond to different $\kappa_{\rm rot}$ (left) and $P(\rm Late)$ (right) values, as

indicated by the colour scale. Clearly, for both types of morphological measurement, late-type galaxies typically retain a higher fraction of their host haloes' specific angular momenta than early-type galaxies.

The precise behaviour of the f_j–M_* curves in Fig. 4 is somewhat dependent on the morphological parameter used. In the case of kinematic morphology (left-hand panel), the retained fraction of angular momentum is remarkably constant for each galaxy type across a wide range of stellar masses, with median values $f_j \approx 0.5$–0.6 for spirals ($\kappa_{\rm rot} \gtrsim 0.6$) and $f_j \approx 0.1$–0.2 for ellipticals ($\kappa_{\rm rot} \approx 1/3$). These values are consistent with observations showing $f_j \approx 0.7$–0.8 for highly disc-dominated galaxies (Fall & Romanowsky 2013; Posti et al. 2019b; Di Teodoro et al. 2021) and $f_j \approx 0.1$ for highly bulge-dominated galaxies (Fall & Romanowsky 2013, 2018). Our f_j measurements from IllustrisTNG are also broadly consistent with results from other hydrodynamic simulations for both spiral and elliptical galaxies (Genel et al. 2015; Pedrosa & Tissera 2015; Teklu et al. 2015; Zavala et al. 2016; Sokołowska et al. 2017; El-Badry et al. 2018).

When splitting galaxies according to visual-like morphology (right-hand panel of Fig. 4), some differences arise with respect to kinematic morphology. One of them is that the range of f_j values becomes smaller, especially at low masses. This effect, which is also visible on the right-hand panel of Fig. 3, could result from the neural network having some difficulty in identifying early types at low masses. In addition, it is to some degree expected that j_* should correlate more strongly with $\kappa_{\rm rot}$ than with any image-based statistic, since both j_* and $\kappa_{\rm rot}$ are kinematic measurements based on the 3D velocities of the stellar particles – information that is unavailable to the neural network.

Another difference between the two panels in Fig. 4 is that the galaxies classified as late types according to $P(\rm Late)$ show a decrease in f_j at high masses. In this case, one should note that this happens at *very* high stellar masses, $\log_{10}(M_*/{\rm M}_\odot) \gtrsim 11.5$, where spirals would be exceedingly rare in the real Universe (or even in the simulation, according to the $\kappa_{\rm rot}$ parameter). Therefore, any results based on $P(\rm Late)$ classifications should be taken with caution at such high
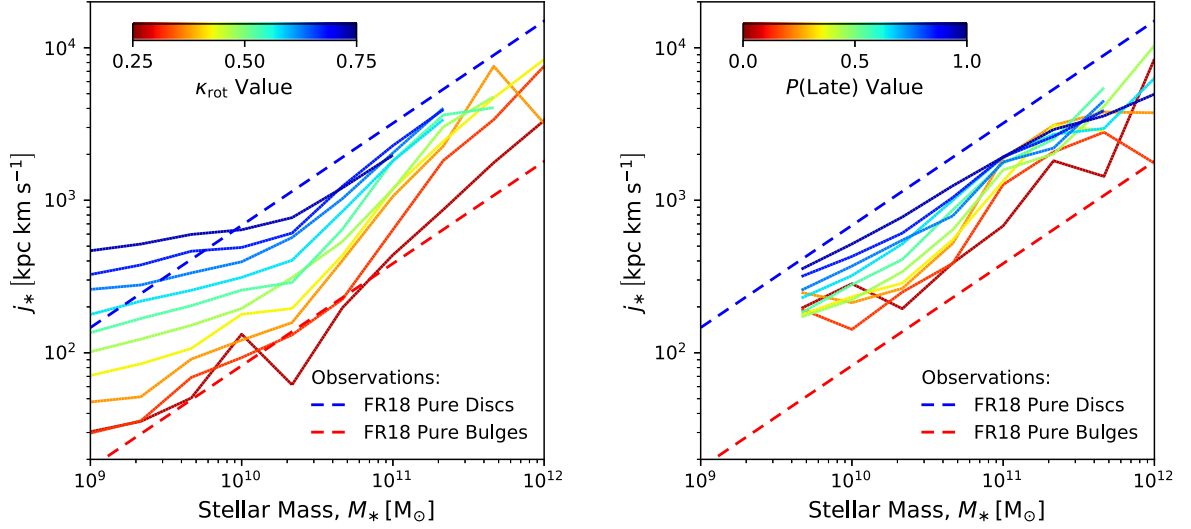
Figure 3. Same as Fig. 2, but separating galaxies according to the actual values of κ_{rot} (left) and P(Late) (right), as indicated by the colour scale, instead of using percentiles at a fixed stellar mass. While the results for P(Late) are relatively unchanged compared to Fig. 2, the j_*-M_* trends for different κ_{rot} values now show a bend near $M_* \sim 2$–$3 \times 10^{10} \, M_\odot$, such that the logarithmic slope becomes shallower than 2/3 at low masses and slightly steeper than 2/3 at the massive end.
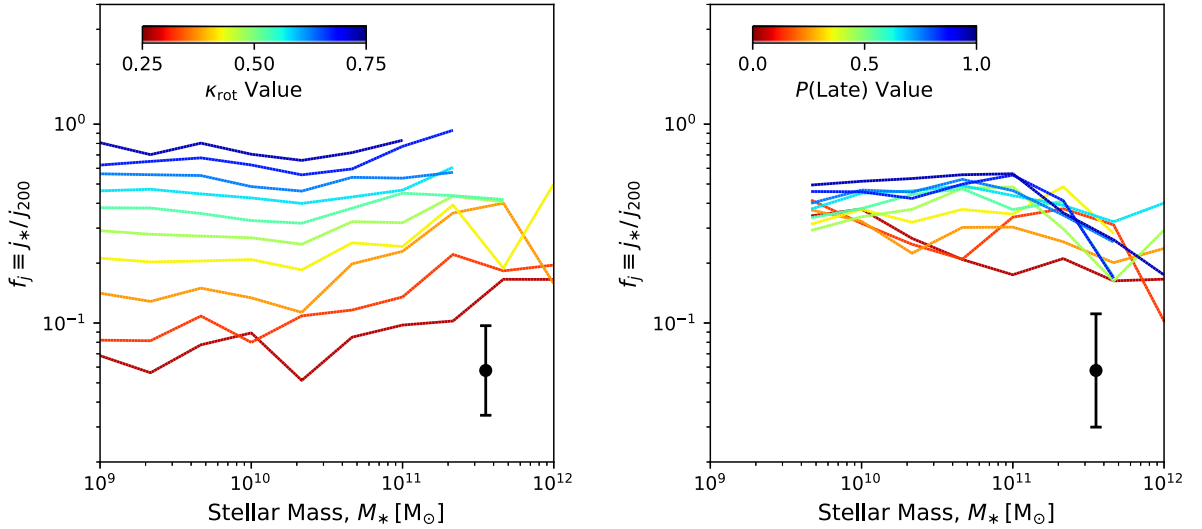
Figure 4. The specific angular momentum 'retention fraction' ($f_j \equiv j_*/j_{200}$) plotted against stellar mass (M_*) for IllustrisTNG central galaxies at $z = 0$. The different coloured lines correspond to different actual values of κ_{rot} (left) and P(Late) (right), as indicated by the colour scale. The error bar in the lower right-hand corner of each panel shows the typical scatter, defined as the median of the 16th to 84th percentile range (in logarithmic units) of all the data points in the figure. Note that when measuring galaxy morphology with the κ_{rot} parameter (left-hand panel), the f_j distributions become remarkably constant across a wide range of stellar masses, with median values $f_j \approx 0.5$–0.6 for spiral galaxies ($\kappa_{rot} \gtrsim 0.6$) and $f_j \approx 0.1$–0.2 for ellipticals ($\kappa_{rot} \approx 1/3$).

masses. Additionally, these f_j trends become approximately constant at $M_* \lesssim 2 \times 10^{11} \, M_\odot$, which makes them qualitatively consistent with the f_j trends for κ_{rot}-selected galaxies, as long as the spirals are limited to a realistic range of stellar masses.

The flatness of the f_j–M_* trends in Fig. 4 has interesting implications for the galaxy–halo connection. While Romanowsky & Fall (2012) favoured a nearly constant value of f_j across all stellar masses, Posti et al. (2018a) argued that the f_j–M_* relation should show an 'inverted U' shape with a peak around $\log_{10}(M_*/M_\odot) \sim 10.5$, which we do not see in Fig. 4. This prediction was obtained by enforcing agreement both with the Fall relation ($j_* \propto M_*^{2/3}$) and

with an inverted-U-shaped stellar-to-halo mass ratio, $f_M \equiv M_*/M_{200}$, for galaxies of all morphological types from Rodríguez-Puebla et al. (2015).

In a subsequent work, Posti et al. (2019a) found that f_M is, in fact, a monotonically increasing function of M_* for spiral galaxies, with no sign of decline at high masses. This finding solves the inconsistency previously pointed out by Posti et al. (2018a), as discussed in Posti et al. (2019b) and Posti & Fall (2021). According to their statistically favoured model (a single power law), Posti et al. (2019b) found a nearly constant value of $f_j \approx 0.7$ for their entire sample of spiral galaxies, with a very weak dependence on stellar mass. This result
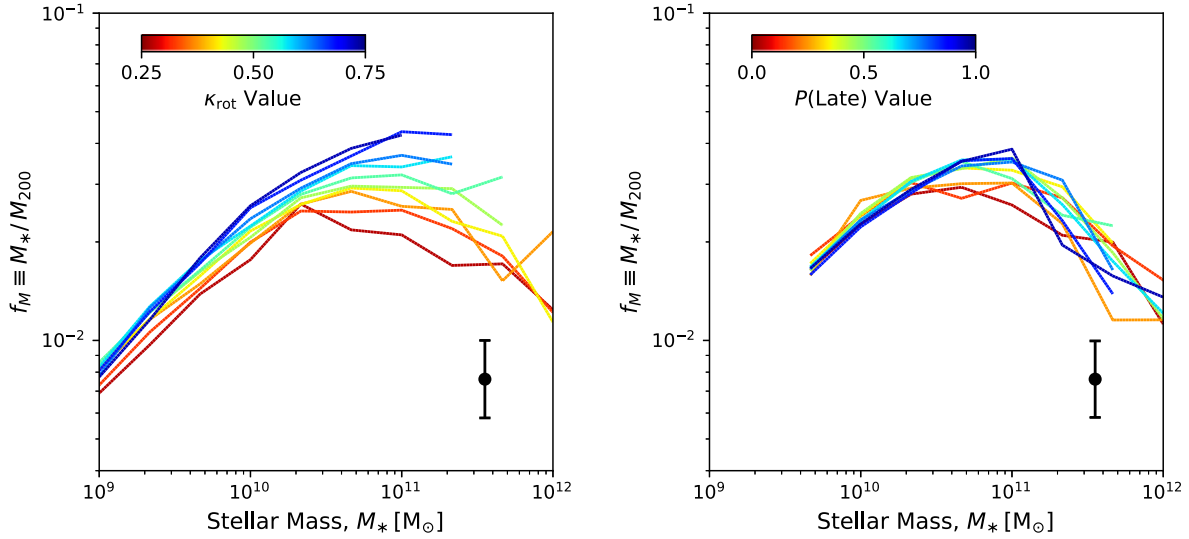
Figure 5. The stellar-to-halo mass ratio ($f_M \equiv M_*/M_{200}$) as a function of stellar mass (M_*) for IllustrisTNG central galaxies at $z = 0$. As before, the different coloured lines represent different actual values of κ_{rot} (left) and $P(\text{Late})$ (right), as indicated by the colour scale, while the error bar in the lower right-hand corner shows the typical scatter. Note that when separating galaxies according to the κ_{rot} parameter (left-hand panel), the f_M–M_* relation is monotonically increasing for spirals ($\kappa_{rot} \gtrsim 0.6$) and inverted-U-shaped for ellipticals ($\kappa_{rot} \approx 1/3$), in qualitative agreement with recent works by Posti, Fraternali & Marasco (2019a) and Posti & Fall (2021).
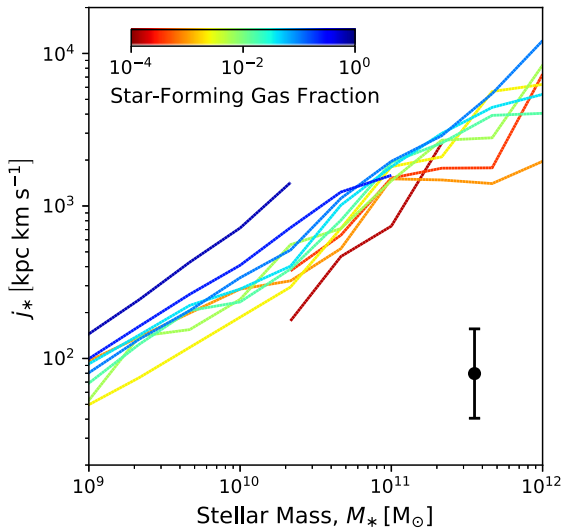
Figure 6. Stellar specific angular momentum (j_*) as a function of stellar mass (M_*) for IllustrisTNG central galaxies at $z = 0$, separating them according to their star-forming gas fraction, $f_{gas, sf} \equiv M_{gas,sf}/(M_{gas,sf} + M_*)$. The error bar in the lower right corner indicates the typical scatter. This figure confirms that, at fixed stellar mass, gas-rich galaxies tend to have higher stellar angular momentum content than gas-poor galaxies, in qualitative agreement with recent works by Mancera Piña et al. (2021b) and Hardwick et al. (2022).

has been confirmed with a larger sample of galaxies by Di Teodoro et al. (2021). Our Fig. 4 provides strong support to this scenario, in which spiral galaxies 'inherit' a fixed fraction, on average, of their parent haloes' specific angular momenta, with similar findings for ellipticals.

For completeness, in Fig. 5 we plot the stellar-to-halo mass ratio ($f_M \equiv M_*/M_{200}$) as a function of stellar mass for central galaxies at $z = 0$. As before, the left-hand and right-hand panels separate galaxies according to the κ_{rot} and $P(\text{Late})$ morphological measurements,

respectively. We can see that when separating galaxies according to $P(\text{Late})$ (right-hand panel), the f_M–M_* relation has approximately the same shape for all morphological types, in qualitative agreement with the semi-empirical model of Rodríguez-Puebla et al. (2015). On the other hand, when classifying galaxies according to κ_{rot} (left-hand panel), $f_M(M_*)$ is monotonically increasing for spirals and inverted-U-shaped for ellipticals, in qualitative agreement with recent works by Posti et al. (2019a) and Posti & Fall (2021), respectively. A closer inspection of the f_M–M_* trend for spirals, however, shows a slight bend at $M_* \gtrsim 10^{10} \, M_\odot$, coming close but not quite matching the single power law favoured by Posti et al. (2019a). This slight bend is the main reason for the corresponding bend in the j_*–M_* trend for spirals previously seen in Fig. 3, which follows from the basic relation[4]

$$j_* \propto f_j f_M^{-2/3} M_*^{2/3} \lambda \qquad (7)$$

by noting that f_j is approximately constant for the different morphological types and that λ is independent of mass.

Finally, motivated by recent observations by Mancera Piña et al. (2021b) and Hardwick et al. (2022), in Fig. 6 we investigate whether the scatter in the j_*–M_* plane is related to the cold gas fraction. As a proxy for cold gas, we consider the mass contributed by all the star-forming gas cells, $M_{gas,sf}$ (see Section 2.2), and then define the star-forming gas fraction as $f_{gas,sf} \equiv M_{gas,sf}/(M_{gas,sf} + M_*)$. Thus, Fig. 6 shows the j_*–M_* trends for galaxies with different values of $f_{gas,sf}$, as indicated by the colour scale. We conclude from this figure that the observed correlation between stellar specific angular momentum and cold gas fraction (at fixed stellar mass) is qualitatively reproduced by the IllustrisTNG model. We note, however, that the dependence of the j_*–M_* relation on cold gas fraction, while significant, is weaker than the dependence on galactic morphology (compare Figs 2, 3, and 6).

---

[4]For the coefficient of proportionality in equation (7), see Romanowsky & Fall (2012) or Posti et al. (2018a).
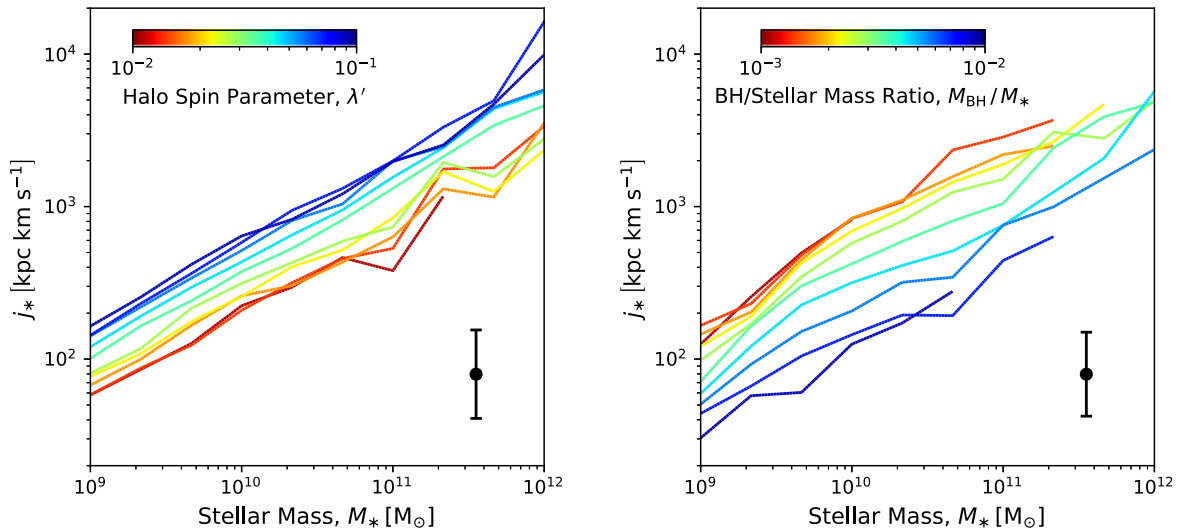
Figure 7. Stellar specific angular momentum (j_*) plotted against stellar mass (M_*) for central galaxies at $z = 0$, separating galaxies according to the spin parameter of their host haloes (left) and the mass of their central BHs (right). Each coloured line shows the median j_*–M_* trend for galaxies with the value indicated by the colour scale. The error bar in the lower right-hand corner of each panel shows the typical scatter. This figure shows that galaxies found at the centres of faster rotating haloes, as well as galaxies hosting less massive BHs, tend to have a higher angular momentum. In addition, the effects of halo spin and BH mass have approximately the same importance at all stellar masses, separating galaxies into roughly parallel tracks on the j_*–M_* diagram.

3.2 Connection to halo spin and BH mass

In this section, we explore what drives the scatter in the j_*–M_* relation, focusing on two important physical quantities: the spin of the host halo and the mass of the supermassive BH at the galactic centre (which we use as a proxy for the amount of energy injected by AGN feedback into the gas over a galaxy's history). We also explore whether there is a correlation between these two quantities, independently of j_*, and whether they play a role in shaping galaxy morphology.

Fig. 7 once again shows how IllustrisTNG galaxies distribute on the j_*–M_* plane at $z = 0$, but in this case the different coloured lines correspond to different values of the halo spin parameter (left) and the BH mass (right). As mentioned in Section 2.3, instead of using the original spin parameter definition by Peebles (1969), we use a very similar one by Bullock et al. (2001), which is usually denoted by λ' instead of λ. The differences between these two quantities have been discussed in various works (e.g. Zjupa & Springel 2017) and are usually of the order of 10 per cent. In the case of the BH mass, we normalize it by the galaxy's stellar mass (M_{BH}/M_*) in order to create a more stable, dimensionless quantity that only spans approximately one order of magnitude across approximately three orders of magnitude in stellar mass. Fig. 7 clearly shows that both halo spin and BH mass are correlated with galactic angular momentum: galaxies that form inside haloes with higher (lower) spin, as well as galaxies hosting less (more) massive BHs at their centres, tend to have higher (lower) values of j_*.

The relation between j_* and halo spin parameter (λ') shown in Fig. 7 has important implications for galaxy formation (Fall & Efstathiou 1980; Mo et al. 1998). It means that galaxy rotation (measured by j_*) depends on halo rotation (measured by λ'), which implies that galaxy sizes should correlate with halo spin, as we will show in Section 3.3. We note that a correlation between j_* and halo spin had been previously found in other hydrodynamic cosmological simulations, in particular by Genel et al. (2015) and Teklu et al. (2015) for the Illustris and Magneticum Pathfinder simulations, respectively.

The relation between j_* and BH mass (M_{BH}) shown in Fig. 7 is less straightforward to interpret. First of all, we note that such a

relation is expected on purely empirical grounds, regardless of the underlying physical process: M_{BH} is known to correlate with bulge mass (e.g. Kormendy & Ho 2013), which anticorrelates with j_* at fixed M_* (e.g. Romanowsky & Fall 2012). The physical link between M_{BH} and bulge mass is believed to be AGN feedback, mergers, or some combination of both processes. However, while galaxy mergers (especially 'dry' mergers) are known to contribute to bulge mass growth (e.g. Rodriguez-Gomez et al. 2017, and references therein), a preliminary analysis suggests that mergers play a less significant role than AGN feedback in establishing the j_*–M_* relation (Rodriguez-Gomez et al., in preparation).

A plausible explanation for the effect of AGN feedback on galactic angular momentum is that AGN feedback acts mostly at late times, suppressing late-time gas accretion in galaxies with more massive BHs. Since the gas accreted at late times has higher specific angular momentum, the lack of it would explain why galaxies with higher M_{BH} have lower j_*. In this sense, the effect of AGN feedback on galactic angular momentum is opposite to that of stellar feedback (e.g. Übler et al. 2014), which favours late-time, favourably oriented gas accretion via galactic fountains. The complementary roles of AGN and stellar feedback in establishing galactic angular momentum are also evident in Genel et al. (2015), who plotted the j_*–M_* relation for several variations of the original Illustris model (Vogelsberger et al. 2013; Torrey et al. 2014) and found that the inclusion of galactic winds increased j_* at fixed M_*, while a model with stronger AGN feedback produced galaxies with lower j_*. Furthermore, using hydrodynamic zoom-in simulations of Milky Way-like galaxies, Grand et al. (2017) found an anticorrelation between disc size and BH mass growth since $z = 1$, which is fundamentally the same effect.

At this point, one might wonder whether the variations in j_* (at fixed M_*) with respect to λ' and M_{BH} seen in Fig. 7 are independent of each other. To check this, in Fig. 8 we plot the joint distribution of the halo spin parameter (horizontal axis) and the BH-to-stellar mass ratio (vertical axis), while colouring each 2D bin according to the median value of $j_*/M_*^{2/3}$. This last quantity is a proxy for j_* that captures its approximate scaling with M_*, essentially quantifying the normalization of the corresponding $j_* \propto M_*^{2/3}$ track (similar to
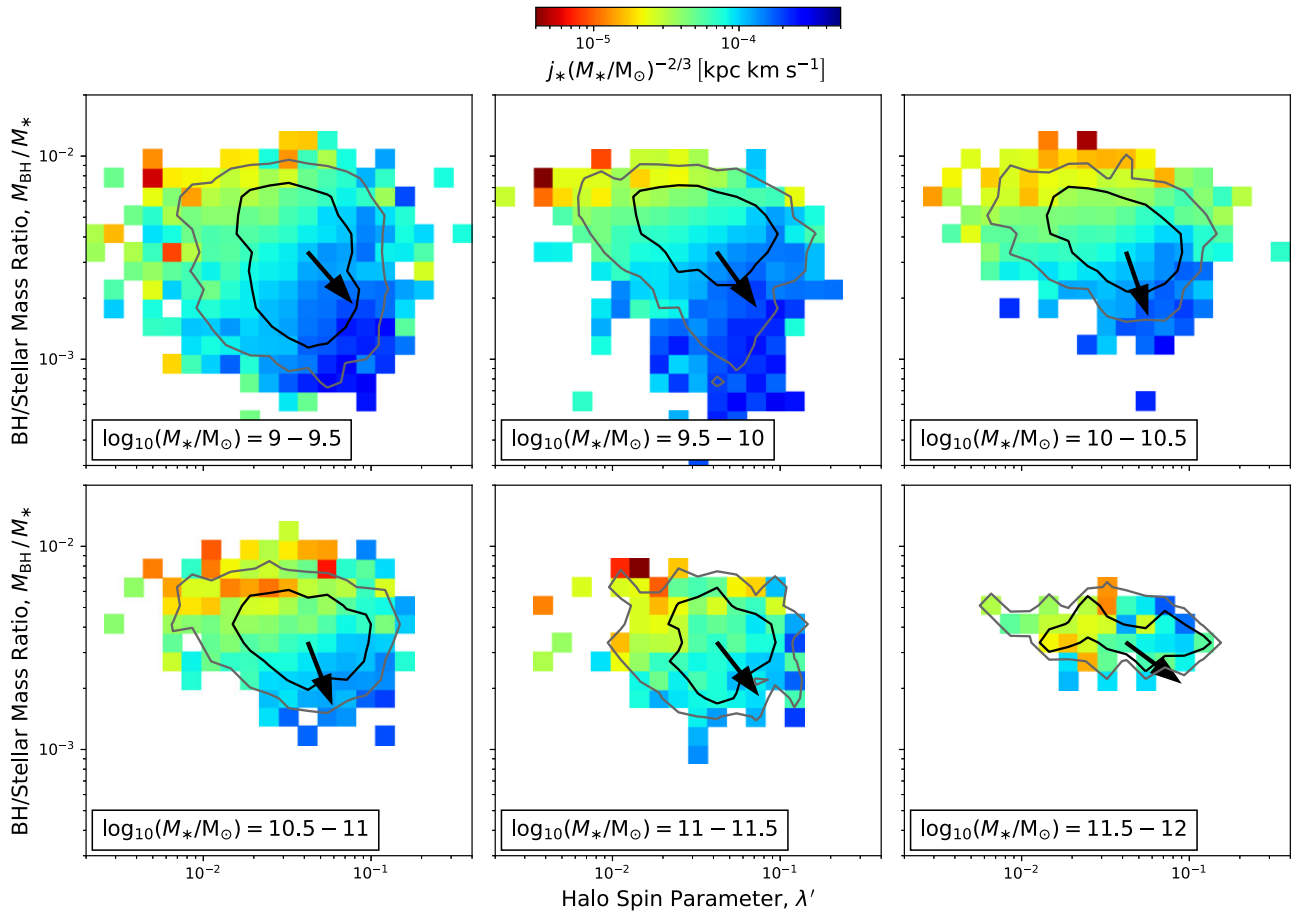
Figure 8. Variation of the stellar specific angular momentum (colour scale) with respect to the halo spin parameter (*x*-axis) and the BH-to-stellar mass ratio (*y*-axis), shown for central galaxies at $z = 0$ in different stellar mass bins (different panels). The stellar specific angular momentum j_* has been divided by $M_*^{2/3}$, its approximate scaling on the j_*–M_* diagram, so that each panel covers a similar range of values. Thus, each two-dimensional bin is coloured according to the median value of $j_*/M_*^{2/3}$ of the galaxies that fall into that bin. The black and grey contours contain 68 and 95 per cent of the galaxy population in each panel, respectively, while the black arrows represent the direction of increasing $j_*/M_*^{2/3}$. Clearly, the colour gradient is approximately diagonal in each panel, which indicates that both halo spin and BH mass are important in establishing galactic angular momentum, regardless of stellar mass.
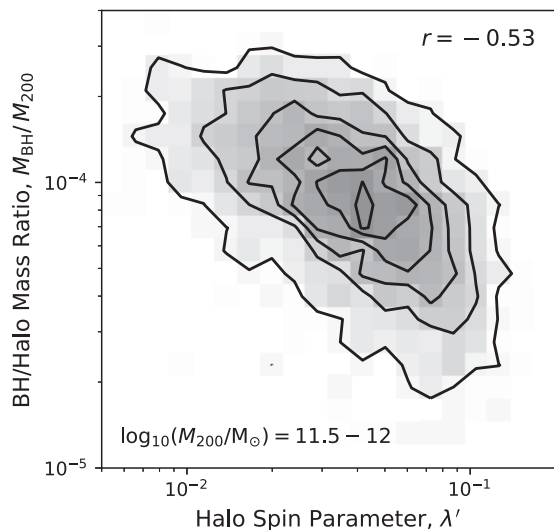
the 'b-values' from Teklu et al. 2015). The different panels show galaxies from different stellar mass ranges, as indicated by the text labels, and the black and grey contours contain 68 and 95 per cent of the galaxy population in each panel.

Examining the direction of the colour gradient (indicated by the black arrows) in each panel of Fig. 8, in combination with the overall shape of the galaxy distribution (grey and black contours), provides information about the relative importance of halo spin and AGN feedback in establishing galactic angular momentum. The fact that the colour gradients are predominantly diagonal (rather than horizontal or vertical) in all panels indicates that both halo spin and AGN feedback play an important role in determining the stellar specific angular momentum of a galaxy, regardless of stellar mass. In other words, any panel from Fig. 8 shows that even at fixed λ', more (less) massive BHs are associated with lower (higher) j_* values. Similarly, at fixed $M_{\rm BH}/M_*$, faster (slower) rotating haloes host galaxies with higher (lower) j_* at their centres.[5]

Close inspection of the contours in Fig. 8 reveals that there is also a connection between halo spin and BH mass, which deserves further attention. This correlation becomes more evident if we essentially bypass the galaxy and replace the ratio $M_{\rm BH}/M_*$ with $M_{\rm BH}/M_{200}$, i.e. if we consider only halo- and BH-related properties. This is done in Fig. 9, which shows the joint distribution of $M_{\rm BH}/M_{200}$ and λ' for a range of halo masses $M_{200} = 10^{11.5}$–10^{12} M$_\odot$. This is roughly the mass range where we find the correlation to be strongest, with a Pearson correlation coefficient of $r = -0.53$ (for the logarithms of $M_{\rm BH}/M_{200}$ and λ'), although we verified that such a correlation exists for all sufficiently massive haloes, with $M_{200} \gtrsim 10^{11}$ M$_\odot$. We find that such a relation is also present in the original Illustris simulation, although it is somewhat weaker, with a Pearson correlation coefficient of $r = -0.33$ for the same halo mass range.

This inverse relation between halo spin and BH mass is likely a consequence of the higher centrifugal acceleration in faster rotating haloes that hinders gas flow to the galactic centre, thus inhibiting the growth of the central BH. Recently, also using the TNG100 simulation, Lu et al. (2022) found decreased star formation activity and lower BH accretion rates in galaxies at the centres of faster spinning haloes, which they also attributed to less efficient gas inflow in these systems. These findings lead to a picture in which the supermassive BHs to some extent 'amplify' the effect of halo spin

---

[5]We also checked the halo concentration, but found that it does not correlate significantly with j_* or $M_{\rm BH}$. However, we found that the halo concentration anticorrelates slightly with halo spin, an effect usually attributed to haloes out of equilibrium (Maccio et al. 2007).

Figure 9. The correlation between BH mass (y-axis, normalized by M_{200}) and halo spin (x-axis) at $z = 0$. This plot is limited to central galaxies within a relatively narrow range of host halo masses ($M_{200} = 10^{11.5}$–10^{12} $M_\odot$), which is approximately where we found the correlation to be strongest, although such a connection to the BH mass exists for all sufficiently massive haloes ($M_{200} \gtrsim 10^{11}$ $M_\odot$) in IllustrisTNG. The contours contain 5, 20, 40, 60, 80, and 95 per cent of the galaxies, while the grey-scale shows their overall distribution. The Pearson correlation coefficient r of the data (in logarithmic units) is indicated in the upper right corner of the figure.

on galactic angular momentum: galaxies with lower j_* form at the centres of haloes with lower λ', but the lower centrifugal acceleration in such haloes results in stronger gas accretion towards the central BH, which contributes to further decreasing j_* via AGN feedback.

When interpreting these results, it is important to note that the process of accretion on to supermassive BHs takes place at scales much smaller than the spatial resolution of current cosmological and galaxy-scale simulations. For example, the 'radius of influence' of supermassive BHs, $r_{\rm infl} \equiv GM_{\rm BH}/\sigma^2$ (where σ is the velocity dispersion of the galactic bulge), has typical values between 1 and 100 pc, much below the $\sim$kpc resolution of TNG100. Furthermore, at even smaller scales, the angular momentum transport mechanisms that funnel gas from the interstellar medium into the BH accretion disc (of size $\lesssim 0.01$ pc) are not fully understood (e.g. Hopkins et al. 2022, and references therein). Despite these issues, the fact that the BH accretion model adopted in IllustrisTNG is coarse (see Section 2.2) does not mean that it is unphysical. In particular, it still seems plausible that low-angular-momentum gas can flow more efficiently towards the central BH than high-angular-momentum gas, regardless of the details of how this gas is transported at subresolution scales.

Having seen that both halo spin and AGN feedback have an effect on galactic angular momentum, one might wonder whether they also have an effect on galaxy morphology. This is tested in Fig. 10, which shows the halo spin parameter (left) and the BH-to-stellar mass ratio (right) as a function of stellar mass, separating galaxies into early types and late types according to the two morphological quantities described in Section 2.4. The solid lines and shaded regions show the median and scatter of $\kappa_{\rm rot}$-selected early types (red) and late types (blue), as indicated by the figure labels, while the dotted lines show the median trends for late-type and early-type galaxies selected according to $P(\text{Late})$.

The right-hand panel of Fig. 10 clearly shows that BH mass is correlated with galaxy morphology at all stellar masses, with

early-type (late-type) galaxies hosting more (less) massive BHs. This is an expected result of the AGN feedback implementation in IllustrisTNG, which heats the gas surrounding a galaxy, suppressing late-time gas accretion and hence the formation of galactic discs, although galaxy mergers are also expected to play a role at the high-mass end (Rodriguez-Gomez et al. 2017). A similar correlation between galaxy morphology and BH mass in IllustrisTNG was found by Li et al. (2020). These findings are qualitatively consistent with the well-known scaling relation between BH mass and bulge mass (e.g. Kormendy & Ho 2013).

On the other hand, the left-hand panel of Fig. 10 shows a negligible correlation between halo spin and galaxy morphology at all inspected masses, which might seem puzzling considering that we find a strong correlation between morphology and j_* (Figs 1–3), as well as between j_* and λ' (Figs 7–8). The reason for this apparent contradiction is that kinematic morphological measurements such as $\kappa_{\rm rot}$ are more strongly correlated with the *inner* j_* (Rodriguez-Gomez et al. 2017), while the halo spin parameter is more strongly correlated with the *outer* j_*. This can lead to a situation where j_* is strongly correlated with both $\kappa_{\rm rot}$ and λ', while these two quantities are very weakly correlated with each other.

Some previous works have reported a correlation between halo spin and morphology in hydrodynamic cosmological simulations, such as Teklu et al. (2015) for the Magneticum Pathfinder simulation and Rodriguez-Gomez et al. (2017) for the original Illustris simulation (at low masses). Regarding the latter case, one possible explanation for why we do not see this effect in IllustrisTNG could be the fact that Illustris galaxies were larger by a factor of $\sim$2, especially at the low-mass end (Snyder et al. 2015; Pillepich et al. 2018a; Rodriguez-Gomez et al. 2019), which could make them more 'dynamically connected' to their parent DM haloes by having an approximately eight times larger 'effective volume' in common. In addition, as a consequence of weaker stellar feedback, the stellar masses in Illustris were higher by a factor of $\sim$2 at the low-mass end, suggesting that stellar angular momentum could also have been affected.

3.3 Halo spin and galaxy size

A well-known prediction of galaxy formation models is that the size of a galactic disc should be correlated to the spin of its parent halo (Fall & Efstathiou 1980; Mo et al. 1998). In Fig. 11, we investigate whether such a relation exists in IllustrisTNG by plotting galaxy size as a function of stellar mass for central galaxies at $z = 0$. The left-hand panel quantifies galaxy size in a very straightforward manner, using the (3D) stellar half-mass radius, while the right-hand panel follows a more observationally motivated approach, showing the half-light semimajor axis obtained from 2D Sérsic fits to the galaxy light distribution in the Pan-STARRS i-band (Rodriguez-Gomez et al. 2019). The coloured solid lines represent different values of the halo spin parameter in logarithmically spaced bins, as indicated by the colour scale. Clearly, a correlation between galaxy size and halo spin exists in IllustrisTNG, at least at stellar masses $M_* \lesssim 10^{11}$ $M_\odot$, with larger discs forming at the centres of faster rotating haloes. Such a relation had been previously found using hydrodynamic zoom-in simulations of Milky Way-like galaxies (Grand et al. 2017).[6] However, this is the first time, to our knowledge, that this correlation has been shown to appear naturally in a fully cosmological volume.

---

[6]Some hydrodynamic zoom-in simulations produce a weaker correlation between galaxy size and halo spin (Jiang et al. 2019). The origin of this discrepancy will be clarified in future work.
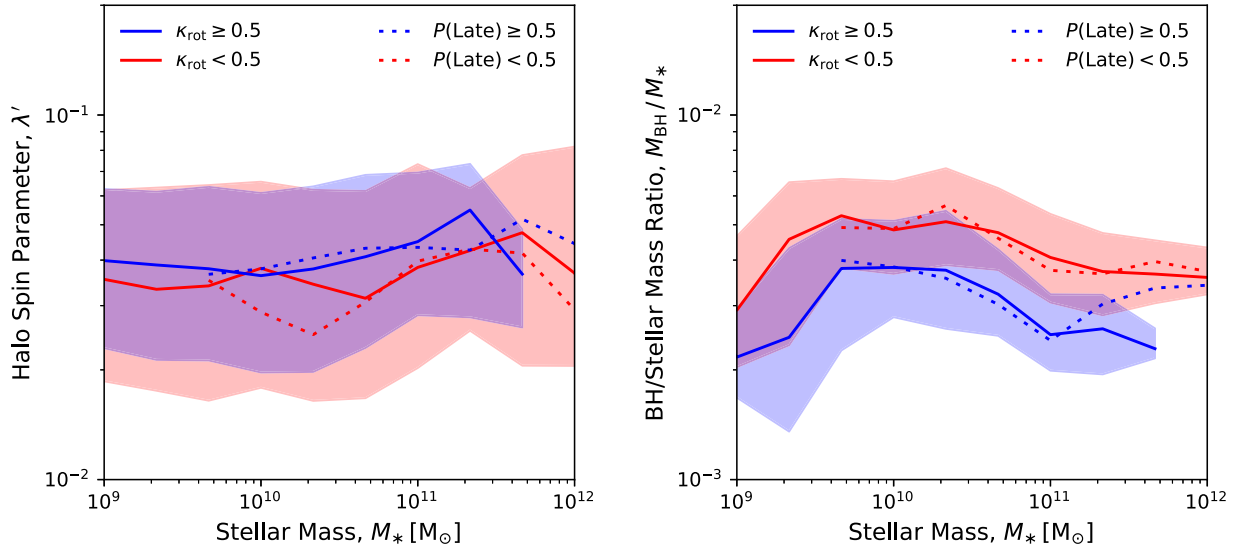
Figure 10. The effect of halo spin (left) and BH mass (right) on galaxy morphology as a function of stellar mass, again shown for central galaxies at $z = 0$. The red and blue solid lines show the median trends for early-type and late-type galaxies, respectively, classified according to *kinematic* morphology (κ_{rot}), while the shaded regions indicate the corresponding 16th to 84th percentile ranges. Similarly, the red and blue dotted lines show the median trends for early-type and late-type galaxies classified according to *visual-like* ($P(\text{Late})$) morphology. This figure shows that, in the IllustrisTNG simulation, halo spin has a marginal effect on galaxy morphology, while BH mass plays a more important role.
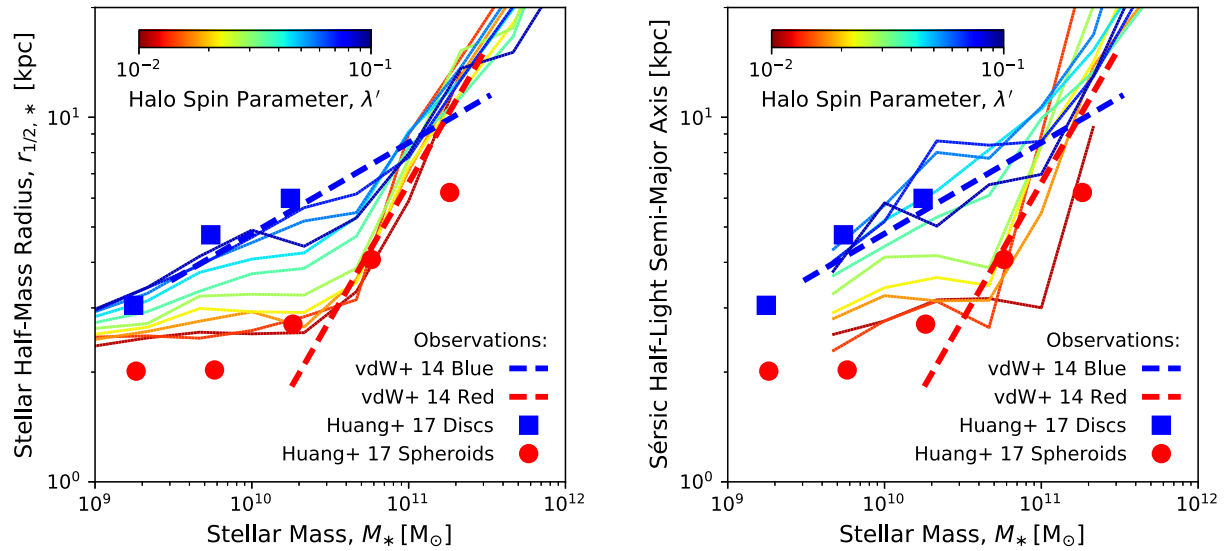
Figure 11. Galaxy size, parametrized by the (3D) stellar half-mass radius (left) and the (2D) Sérsic half-light semimajor axis (right), plotted against stellar mass for central galaxies at $z = 0$. The different solid coloured lines show median trends for galaxies found at the centres of haloes with different spin parameters, as indicated by the colour scale. The blue squares and red circles show the median observational trends from Huang et al. (2017) for disc-dominated and spheroid-dominated galaxies, respectively, while the dashed lines represent power-law fits by van der Wel et al. (2014) for blue and red galaxies. This figure shows that larger galaxies formed at the centres of faster rotating haloes, in agreement with simple analytical arguments, and that the variations in halo spin span the observed range of morphologies and colours. However, the trend breaks down at $M_* \gtrsim 10^{11}\,\mathrm{M_\odot}$ in both observations and simulations, presumably as a result of the increased importance of dry mergers in the formation of massive galaxies and the associated destruction of galactic discs.

We complement Fig. 11 by also showing observational determinations of the effective size versus stellar mass relation for different galaxy types. The blue squares and red circles represent median observational trends obtained by Huang et al. (2017) for disc-dominated and spheroid-dominated galaxies, respectively, using data from the CANDELS survey (Grogin et al. 2011; Koekemoer et al. 2011) at $z < 0.5$. Similarly, the blue and red dashed lines show power-law fits by van der Wel et al. (2014) for blue and red galaxies (selected according to their rest-frame UVJ colours), using the same

CANDELS measurements at $z < 0.5$. Interestingly, this comparison shows that the variations in the spin of the DM halo span the observed range of galaxy morphologies and colours, again suggesting that halo spin plays a significant role in galaxy formation, as discussed in Section 3.2.

The connection between halo spin and galaxy size is closely related to the idea that low surface brightness galaxies (LSBGs), as well as ultradiffuse galaxies (UDGs), might form at the centres of faster spinning haloes (Amorisco & Loeb 2016; Pérez-Montaño

& Cervantes Sodi 2019; Salinas & Galaz 2021). These tendencies for LSBGs and (isolated) UDGs have been recently verified using hydrodynamic simulations (Di Cintio et al. 2019; Kulier et al. 2020; Benavides et al. 2021; Pérez-Montaño et al., in preparation).

As also shown in Fig. 11, the correlation between galaxy size and halo spin breaks down at $M_* \gtrsim 10^{11}\,\mathrm{M_\odot}$ in both observations and simulations, which is perhaps not surprising considering that the theoretical prediction is for galactic *discs*, while the high-mass end is dominated by elliptical galaxies. This transition at $M_* \sim 10^{11}\,\mathrm{M_\odot}$ roughly corresponds to the mass scale at which dry mergers become the dominant growth mechanism of galaxies (Lee & Yi 2013; Rodriguez-Gomez et al. 2016), driven mostly by the effectiveness of AGN feedback in massive galaxies and their consequent quenching, leading to the formation of spheroid-dominated systems at the massive end (Rodriguez-Gomez et al. 2017). Genel et al. (2018) also noted a different size evolution for galaxies above and below this mass scale, such that the sizes of galaxies with $M_* \gtrsim 10^{11}\,\mathrm{M_\odot}$ at $z = 0$ showed very slow growth after quenching. In future work, we will explore the role that galaxy mergers play in establishing galactic angular momentum at different masses.

4 DISCUSSION AND CONCLUSIONS

We have studied the stellar specific angular momenta (j_*) of central galaxies in the IllustrisTNG simulation at $z = 0$, covering a stellar mass range from 10^9 to $10^{12}\,\mathrm{M_\odot}$, with an emphasis on how j_* relates to the morphology of the galaxy, the spin of the host halo, and the mass of the central BH. We also explored the fraction of the halo specific angular momentum 'retained' by galaxies of different morphological types, and tested whether a connection between halo spin and galaxy size, which is predicted by simple analytical arguments, arises naturally in a cosmological context.

We quantified the morphology of our simulated galaxies using two different indicators: the $\kappa_{\rm rot}$ parameter (Sales et al. 2010; Rodriguez-Gomez et al. 2017), which measures the fraction of kinetic energy of the stars that is invested into ordered circular motion, and $P(\rm Late)$, which gives the probability that a galaxy has a late-type morphology according to a deep learning algorithm (Huertas-Company et al. 2019). The quantities $\kappa_{\rm rot}$ and $P(\rm Late)$ represent *kinematic* and *visual-like* morphological measurements, respectively, and the simulated galaxies can be roughly separated into early types and late types by adopting cuts at $\kappa_{\rm rot} = 0.5$ and $P(\rm Late) = 0.5$. For both types of morphological measurement, we found that the distribution of IllustrisTNG galaxies on the j_*–M_* plane is in good overall agreement with observational estimates from Fall & Romanowsky (2013) for both early types and late types, and with Posti et al. (2018b) and Di Teodoro et al. (2021) for late types (Fig. 1), with the late types exhibiting higher j_* at fixed galaxy stellar mass.

We further explored the relation between galactic angular momentum and morphology by showing several finely spaced median trends on the j_*–M_* diagram, corresponding to galaxies classified according to the percentile at a fixed stellar mass (Fig. 2) and the actual value (Fig. 3) of the morphological parameters $\kappa_{\rm rot}$ and $P(\rm Late)$. This allowed us to probe the entire range of galaxy morphologies produced by the simulation in more detail. In both cases, we compared the obtained trends with the 3D fits provided by Fall & Romanowsky (2018) for the extreme cases of 'pure' discs and spheroids, which have a logarithmic slope of 2/3 but are separated by a factor of approximately eight in normalization.

We found that when separating morphological types according to the percentile at fixed mass (Fig. 2), the j_*–M_* trends for both $\kappa_{\rm rot}$ and $P(\rm Late)$ behave very similarly to each other, and the range of

j_* values covered by these 'morphological classes' is comparable to the separation between the pure discs and spheroids from Fall & Romanowsky (2018), although with a somewhat smaller spread in the case of $P(\rm Late)$.

When separating galaxies according to the actual values of $\kappa_{\rm rot}$ and $P(\rm Late)$ (Fig. 3), the behaviour for $P(\rm Late)$ is relatively unchanged, but the j_*–M_* trends for different $\kappa_{\rm rot}$ values now deviate from the simple $j_* \propto M_*^{2/3}$ relation favoured by Fall & Romanowsky (2018), displaying instead a bend near $M_* \sim 2$–$3 \times 10^{10}\,\mathrm{M_\odot}$, such that the logarithmic slopes in the j_*–M_* plane at stellar masses above (below) this transition point become steeper (shallower) than 2/3. The main reason for these qualitative differences between Figs 2 and 3 is that galaxy morphology is mass-dependent, with more disc-dominated galaxies at $\log_{10}(M_*/\mathrm{M_\odot}) \sim 10.5$ and more spheroid-dominated galaxies at lower and higher masses.

We next considered the specific angular momentum 'retention fraction', defined as the ratio between the specific angular momenta of the galaxy and its host halo, $f_j \equiv j_*/j_{200}$, and plotted it as a function of stellar mass (Fig. 4). When splitting the simulated galaxies by their $\kappa_{\rm rot}$ values, we found that the resulting f_j trends are remarkably constant as a function of stellar mass, with spiral galaxies ($\kappa_{\rm rot} \gtrsim 0.6$) 'retaining' 50–60 per cent of their host haloes' specific angular momenta and ellipticals ($\kappa_{\rm rot} \approx 1/3$) retaining 10–20 per cent. These values are close to the best empirical estimates of $f_j \approx 0.7$–0.8 for highly disc-dominated galaxies (Fall & Romanowsky 2013; Posti et al. 2019b; Di Teodoro et al. 2021) and $f_j \approx 0.1$ for spheroid-dominated galaxies (Fall & Romanowsky 2013, 2018).

For completeness, we also considered the stellar-to-halo mass ratio ($f_M \equiv M_*/M_{200}$), which is related to j_* via equation (7), and plotted it in Fig. 5 as a function of stellar mass. When separating galaxies according to their $\kappa_{\rm rot}$ values, we found that spirals show a monotonically increasing $f_M(M_*)$, while ellipticals show an 'inverted U' shape, in qualitative agreement with Posti et al. (2019a) and Posti & Fall (2021), respectively. Finally, in Fig. 6 we showed that IllustrisTNG galaxies also display a correlation between j_* and cold gas fraction at fixed M_*, in qualitative agreement with recent observational works by Mancera Piña et al. (2021b) and Hardwick et al. (2022), although the dependence of the j_*–M_* relation on cold gas fraction is weaker than its dependence on galactic morphology.

Having explored the interplay between galactic angular momentum and morphology, we proceeded to investigate the physical mechanisms that drive the scatter in the j_*–M_* relation at fixed M_*. In particular, we considered the spin of the host halo (λ') and the mass of the central BH ($M_{\rm BH}$, which we used as a proxy for the amount of energy injected into the gas by AGN feedback over a galaxy's history). We found that galaxies that formed at the centres of faster (slower) rotating haloes, as well as those hosting less (more) massive BHs, tend to have higher (lower) stellar specific angular momenta (Fig. 7).

We also found that the correlations between galactic angular momentum, halo spin, and BH mass hold at fixed λ' or $M_{\rm BH}/M_*$ (Fig. 8), indicating that halo spin and AGN feedback play distinct roles in driving the scatter of the j_*–M_* relation. This paper supports a scenario where the rotation of a galaxy (measured by j_*) depends on that of its host halo (measured by λ'), while AGN feedback (by suppressing late-time gas accretion, which has higher specific angular momentum) has an effect opposite to that of stellar feedback in establishing galactic angular momentum, in agreement with earlier findings (Genel et al. 2015; Grand et al. 2017).

Interestingly, we also found an anticorrelation between the spin of the halo and the mass of the supermassive BH at fixed galaxy or halo mass (Fig. 9). This could be explained by stronger (weaker)

gas flows feeding the central BH in slower (faster) rotating haloes, where the centrifugal acceleration is easier (harder) to overcome. This would also mean that BHs to some extent 'amplify' the effect of the halo spin: galaxies tend to have lower j_* if they form inside slowly rotating haloes, but such slow rotation leads to increased BH growth and a stronger effect of AGN feedback, further decreasing j_*. It will be interesting and important to check with other simulations whether this prediction holds for models of gas accretion into supermassive BHs that account for the dynamics of the gas in the innermost regions of galaxies, e.g. in the case of the gravitational torque-limited accretion models of the Simba simulation (Davé et al. 2019).

We also studied the effects of halo spin and BH mass on galaxy morphology (Fig. 10). As expected, we found that more massive BHs are associated with earlier type morphologies, in agreement with observations (Kormendy & Ho 2013) as well as with earlier findings using the IllustrisTNG simulation (Li et al. 2020). On the other hand, we found a negligible correlation between halo spin and galaxy morphology, in disagreement with some recent works. In particular, using the original Illustris simulation, Rodriguez-Gomez et al. (2017) found a significant correlation between $\kappa_{\rm rot}$ and λ' at low masses ($M_* \lesssim 10^{10}\,{\rm M_\odot}$), which we do not reproduce with the updated IllustrisTNG model. This could be explained by the significantly larger sizes of low-mass Illustris galaxies (Snyder et al. 2015; Pillepich et al. 2018a; Rodriguez-Gomez et al. 2019), which could lead to increased dynamical interaction with their host haloes, or to the fact that stellar feedback was directional in Illustris but isotropic in IllustrisTNG (Pillepich et al. 2018a).

Finally, we revisited a well-known prediction of some analytical models of galaxy formation: that haloes with a higher spin parameter should form larger discs at their centres (Fall & Efstathiou 1980; Mo et al. 1998). We tested this hypothesis by plotting the galaxy size as a function of stellar mass, showing the median trends for different λ' values (Fig. 11). We verified that there is indeed a correlation between galaxy size and halo spin in IllustrisTNG, which breaks down at the massive end ($M_* \gtrsim 10^{11}\,{\rm M_\odot}$), probably due to the increased importance of galaxy mergers in this regime (Lee & Yi 2013; Rodriguez-Gomez et al. 2016) and the associated change in galaxy morphology, from discs to spheroids (Rodriguez-Gomez et al. 2017). Furthermore, we found that the variations in galaxy size with respect to halo spin span the observed range of galaxy morphologies and colours (van der Wel et al. 2014; Huang et al. 2017).

Overall, we have found that the properties of galactic angular momentum at $z = 0$ in the IllustrisTNG simulation are in good agreement with observational constraints, despite the fact that the IllustrisTNG model was not tuned to match these observations (although it was designed to roughly match galaxy sizes at $z = 0$). We have also investigated how galactic angular momentum relates to morphology, halo spin, and BH mass within this galaxy formation framework. All of this has been possible due to enormous theoretical and computational advances in the last few decades. Further observational data will be needed to test some of the predictions made in this paper, especially kinematic measurements for early-type galaxies at large radii.

On the theoretical side, further progress can be made with additional studies about the redshift evolution of galactic angular momentum, its detailed spatial distribution, its alignment to the gaseous and DM components, and the effect of mergers, which we will address in upcoming work. Furthermore, enhanced and more robust comparisons between theory and observations, such as with forward modelling of integral field spectroscopic observations (Ibarra-Medel et al. 2019; Bouché et al. 2021), will be pivotal in order to constrain and improve future models of galaxy formation.

DATA AVAILABILITY

The data from the Illustris and IllustrisTNG simulations used in this work are publicly available at the websites https://www.illustris-project.org and https://www.tng-project.org, respectively (Nelson et al. 2015, 2019a).

REFERENCES

Abadi M. G., Navarro J. F., Steinmetz M., Eke V. R., 2003, ApJ, 597, 21
Amorisco N. C., Loeb A., 2016, MNRAS, 459, L51
Aumer M., White S. D. M., Naab T., Scannapieco C., 2013, MNRAS, 434, 3142
Avila-Reese V., Firmani C., Hernandez X., 1998, ApJ, 505, 37
Baes M., Verstappen J., De Looze I., Fritz J., Saftly W., Vidal Pérez E., Stalevski M., Valcke S., 2011, ApJS, 196, 22
Barnes J. E., 1988, ApJ, 331, 699
Benavides J. A. et al., 2021, Nat. Astron., 5, 1255
Bondi H., 1952, MNRAS, 112, 195
Bottrell C., Torrey P., Simard L., Ellison S. L., 2017, MNRAS, 467, 2879
Bouché N. F. et al., 2021, A&A, 654, A49
Bullock J. S., Dekel A., Kolatt T. S., Kravtsov A. V., Klypin A. A., Porciani C., Primack J. R., 2001, ApJ, 555, 240
Camps P., Baes M., 2015, Astron. Comput., 9, 20
Chabrier G., 2003, PASP, 115, 763
Cheung E. et al., 2016, Nature, 533, 504
Correa C. A., Schaye J., Clauwens B., Bower R. G., Crain R. A., Schaller M., Theuns T., Thob A. C. R., 2017, MNRAS, 472, L45
Cortese L. et al., 2016, MNRAS, 463, 170
Crain R. A. et al., 2015, MNRAS, 450, 1937
Dalcanton J. J., Spergel D. N., Summers F. J., 1997, ApJ, 482, 659
Davé R., Anglés-Alcázar D., Narayanan D., Li Q., Rafieferantsoa M. H., Appleby S., 2019, MNRAS, 486, 2827
Davis M., Efstathiou G., Frenk C. S., White S. D. M., 1985, ApJ, 292, 371
DeFelippis D., Genel S., Bryan G. L., Fall S. M., 2017, ApJ, 841, 16
Di Cintio A., Brook C. B., Macciò A. V., Dutton A. A., Cardona-Barrero S., 2019, MNRAS, 486, 2535
Di Teodoro E. M., Posti L., Ogle P. M., Fall S. M., Jarrett T., 2021, MNRAS, 507, 5820
Dolag K., Borgani S., Murante G., Springel V., 2009, MNRAS, 399, 497
Donnari M. et al., 2021a, MNRAS, 500, 4004
Donnari M., Pillepich A., Nelson D., Marinacci F., Vogelsberger M., Hernquist L., 2021b, MNRAS, 506, 4760
Doroshkevich A. G., 1970, Astrofizika, 6, 581
Dubois Y., Peirani S., Pichon C., Devriendt J., Gavazzi R., Welker C., Volonteri M., 2016, MNRAS, 463, 3948

Dutton A. A., van den Bosch F. C., 2012, MNRAS, 421, 608
El-Badry K. et al., 2018, MNRAS, 473, 1930
Fall S. M., 1979, Nature, 281, 200
Fall S. M., 1983, in Athanassoula E., ed., IAU Symp. 100, Internal Kinematics and Dynamics of Galaxies. Cambridge Univ. Press, Cambridge, p. 391
Fall S. M., Efstathiou G., 1980, MNRAS, 193, 189
Fall S. M., Romanowsky A. J., 2013, ApJ, 769, L26
Fall S. M., Romanowsky A. J., 2018, ApJ, 868, 133
Faucher-Giguère C.-A., Lidz A., Zaldarriaga M., Hernquist L., 2009, ApJ, 703, 1416
Firmani C., Avila-Reese V., 2000, MNRAS, 315, 457
Firmani C., Avila-Reese V., 2009, MNRAS, 396, 1675
Genel S. et al., 2014, MNRAS, 445, 175
Genel S., Fall S. M., Hernquist L., Vogelsberger M., Snyder G. F., Rodriguez-Gomez V., Sijacki D., Springel V., 2015, ApJ, 804, L40
Genel S. et al., 2018, MNRAS, 474, 3976
Grand R. J. J. et al., 2017, MNRAS, 467, 179
Grand R. J. J. et al., 2019, MNRAS, 490, 4786
Grogin N. A. et al., 2011, ApJS, 197, 35
Hardwick J. A., Cortese L., Obreschkow D., Catinella B., Cook R. H. W., 2022, MNRAS, 509, 3751
Hernquist L., Mihos J. C., 1995, ApJ, 448, 41
Hirschmann M., Dolag K., Saro A., Bachmann L., Borgani S., Burkert A., 2014, MNRAS, 442, 2304
Hopkins P. F., Wellons S., Anglés-Alcázar D., Faucher-Giguère C.-A., Grudić M. Y., 2022, MNRAS, 510, 630
Huang K.-H. et al., 2017, ApJ, 838, 6
Huertas-Company M. et al., 2019, MNRAS, 489, 1859
Ibarra-Medel H. J., Avila-Reese V., Sánchez S. F., González-Samaniego A., Rodríguez-Puebla A., 2019, MNRAS, 483, 4525
Irodotou D., Thomas P. A., Henriques B. M., Sargent M. T., Hislop J. M., 2019, MNRAS, 489, 3609
Jiang F. et al., 2019, MNRAS, 488, 4801
Kassin S. A., Devriendt J., Fall S. M., de Jong R. S., Allgood B., Primack J. R., 2012, MNRAS, 424, 502
Koekemoer A. M. et al., 2011, ApJS, 197, 36
Kormendy J., Ho L. C., 2013, ARA&A, 51, 511
Kulier A., Galaz G., Padilla N. D., Trayford J. W., 2020, MNRAS, 496, 3996
Lacey C. G., Ostriker J. P., 1985, ApJ, 299, 633
Lagos C. D. P., Theuns T., Stevens A. R. H., Cortese L., Padilla N. D., Davis T. A., Contreras S., Croton D., 2017, MNRAS, 464, 3850
Lagos C. D. P. et al., 2018, MNRAS, 473, 4956
Lapi A. et al., 2018a, ApJ, 857, 22
Lapi A., Salucci P., Danese L., 2018b, ApJ, 859, 2
Lee J., Yi S. K., 2013, ApJ, 766, 38
Lewis A., Challinor A., Lasenby A., 2000, ApJ, 538, 473
Li Y. et al., 2020, ApJ, 895, 102
Lu S. et al., 2022, MNRAS, 509, 2707
Ludlow A. D., Fall S. M., Schaye J., Obreschkow D., 2021, MNRAS, 508, 5114
Maccio A. V., Dutton A. A., Van Den Bosch F. C., Moore B., Potter D., Stadel J., 2007, MNRAS, 378, 55
Mancera Piña P. E., Posti L., Fraternali F., Adams E. A. K., Oosterloo T., 2021a, A&A, 647, A76
Mancera Piña P. E., Posti L., Pezzulli G., Fraternali F., Fall S. M., Oosterloo T., Adams E. A. K., 2021b, A&A, 651, L15
Marinacci F. et al., 2018, MNRAS, 5139, 5113
Mo H. J., Mao S., White S. D. M., 1998, MNRAS, 295, 319
Naab T., Ostriker J. P., 2017, ARA&A, 55, 59
Naiman J. P. et al., 2018, MNRAS, 477, 1206
Navarro J. F., Steinmetz M., 1997, ApJ, 478, 13
Navarro J. F., Frenk C. S., White S. D. M., 1995, MNRAS, 275, 56
Nelson D. et al., 2015, Astron. Comput., 13, 12
Nelson D. et al., 2018, MNRAS, 475, 624
Nelson D. et al., 2019a, Comput. Astrophys. Cosmol., 6, 2
Nelson D. et al., 2019b, MNRAS, 490, 3234
Obreja A., Stinson G. S., Dutton A. A., Macciò A. V., Wang L., Kang X., 2016, MNRAS, 459, 467

Obreja A. et al., 2019, MNRAS, 487, 4424
Obreschkow D., Glazebrook K., 2014, ApJ, 784, 26
Pakmor R., Springel V., 2013, MNRAS, 432, 176
Pakmor R., Springel V., Bauer A., Mocz P., Munoz D. J., Ohlmann S. T., Schaal K., Zhu C., 2016, MNRAS, 455, 1134
Pedrosa S. E., Tissera P. B., 2015, A&A, 584, A43
Peebles P. J. E., 1969, ApJ, 155, 393
Pérez-Montaño L. E., Cervantes Sodi B., 2019, MNRAS, 490, 3772
Pillepich A. et al., 2018a, MNRAS, 473, 4077
Pillepich A. et al., 2018b, MNRAS, 475, 648
Pillepich A. et al., 2019, MNRAS, 490, 3196
Planck Collaboration XIII, 2016, A&A, 594, A13
Posti L., Fall S. M., 2021, A&A, 649, A119
Posti L., Pezzulli G., Fraternali F., Di Teodoro E. M., 2018a, MNRAS, 475, 232
Posti L., Fraternali F., Di Teodoro E. M., Pezzulli G., 2018b, A&A, 612, L6
Posti L., Fraternali F., Marasco A., 2019a, A&A, 626, A56
Posti L., Marasco A., Fraternali F., Famaey B., 2019b, A&A, 629, A59
Rodriguez-Gomez V. et al., 2016, MNRAS, 458, 2371
Rodriguez-Gomez V. et al., 2017, MNRAS, 467, 3083
Rodriguez-Gomez V. et al., 2019, MNRAS, 483, 4140
Rodríguez-Puebla A., Avila-Reese V., Yang X., Foucaud S., Drory N., Jing Y. P., 2015, ApJ, 799, 130
Romanowsky A. J., Fall S. M., 2012, ApJS, 203, 17
Sales L. V., Navarro J. F., Schaye J., Vecchia C. D., Springel V., Booth C. M., 2010, MNRAS, 409, 1541
Sales L. V., Navarro J. F., Theuns T., Schaye J., White S. D. M., Frenk C. S., Crain R. A., Dalla Vecchia C., 2012, MNRAS, 423, 1544
Salinas V. H., Galaz G., 2021, ApJ, 915, 125
Salpeter E. E., 1955, ApJ, 121, 161
Scannapieco C., White S. D. M., Springel V., Tissera P. B., 2009, MNRAS, 396, 696
Scannapieco C. et al., 2012, MNRAS, 423, 1726
Schaye J. et al., 2015, MNRAS, 446, 521
Shakura N. I., Sunyaev R. A., 1973, A&A, 24, 337
Shi J., Lapi A., Mancuso C., Wang H., Danese L., 2017, ApJ, 843, 105
Sijacki D., Springel V., Di Matteo T., Hernquist L., 2007, MNRAS, 380, 877
Snyder G. F. et al., 2015, MNRAS, 454, 1886
Sokołowska A., Capelo P. R., Fall S. M., Mayer L., Shen S., Bonoli S., 2017, ApJ, 835, 289
Somerville R. S., Davé R., 2015, ARA&A, 53, 51
Sommer-Larsen J., Gelato S., Vedel H., 1999, ApJ, 519, 501
Springel V., 2005, MNRAS, 364, 1105
Springel V., 2010, MNRAS, 401, 791
Springel V., Hernquist L., 2003, MNRAS, 339, 289
Springel V., Hernquist L., 2005, ApJ, 622, L9
Springel V., White S. D. M., Tormen G., Kauffmann G., 2001, MNRAS, 328, 726
Springel V., Di Matteo T., Hernquist L., 2005, MNRAS, 361, 776
Springel V. et al., 2018, MNRAS, 475, 676
Starkenburg T. K., Sales L. V., Genel S., Manzano-King C., Canalizo G., Hernquist L., 2019, ApJ, 878, 143
Stevens A. R. H., Croton D. J., Mutch S. J., 2016, MNRAS, 461, 859
Tabor M., Merrifield M., Aragón-Salamanca A., Fraser-McKelvie A., Peterken T., Smethurst R., Drory N., Lane R. R., 2019, MNRAS, 485, 1546
Tacchella S. et al., 2019, MNRAS, 487, 5416
Teklu A. F., Remus R.-S., Dolag K., Beck A. M., Burkert A., Schmidt A. S., Schulze F., Steinborn L. K., 2015, ApJ, 812, 29
Thacker R. J., Couchman H. M. P., 2001, ApJ, 555, L17
Torrey P., Vogelsberger M., Sijacki D., Springel V., Hernquist L., 2012, MNRAS, 427, 2224
Torrey P., Vogelsberger M., Genel S., Sijacki D., Springel V., Hernquist L., 2014, MNRAS, 438, 1985
Übler H., Naab T., Oser L., Aumer M., Sales L. V., White S. D. M., 2014, MNRAS, 443, 2092
van den Bosch F. C., 1998, ApJ, 507, 601
van der Wel A. et al., 2014, ApJ, 788, 28
Varma S. et al., 2022, MNRAS, 509, 2654

Vogelsberger M., Genel S., Sijacki D., Torrey P., Springel V., Hernquist L., 2013, MNRAS, 436, 3031

Vogelsberger M. et al., 2014a, MNRAS, 444, 1518

Vogelsberger M. et al., 2014b, Nature, 509, 177

Vogelsberger M., Marinacci F., Torrey P., Puchwein E., 2020, Nat. Rev. Phys., 2, 42

Weinberger R. et al., 2017, MNRAS, 465, 3291

White S. D. M., 1984, ApJ, 286, 38

Yuan F., Narayan R., 2014, ARA&A, 52, 529

Zavala J. et al., 2016, MNRAS, 460, 4466

Zjupa J., Springel V., 2017, MNRAS, 466, 1625

Zoldan A., De Lucia G., Xie L., Fontanot F., Hirschmann M., 2018, MNRAS, 481, 1376

This paper has been typeset from a TEX/LATEX file prepared by the author.